Sulfur in Mesoporous Tungsten Nitride Foam Blocks: a Rational Lithium Polysufides Confinement Experimental Design Strategy Augmented by Theoretical Predictions

Zhen-Dong Huang,[‡, a] *Yanwu Fang,*[‡, a] *Mingtong Yang,*[a] *Jike Yang,*[a] *Yizhou Wang,*[a] *Zhen Wu,*[*, b] *Qingchuan Du,*[a] *Titus Masese,*[*, c] *Ruiqing Liu,*[a] *Xusheng Yang,*[d, e] *Chenhui Qian,*[b] *Shaowei Jin,*[f] *Yanwen Ma*[*a]

[a] Key Laboratory for Organic Electronics and Information Displays & Jiangsu Key Laboratory for Biosensors, Institute of Advanced Materials (IAM), Jiangsu National Synergetic Innovation Center for Advanced Materials (SICAM), Nanjing University of Posts and Telecommunications, 9 Wenyuan Road, Nanjing 210023, P.R. China.

[b] Shaanxi Key Laboratory of Energy Chemical Process Intensification, School of Chemical Engineering and Technology, Xi'an Jiaotong University, Xi'an 710049, P.R. China.

[c] Research Institute of Electrochemical Energy, National Institute of Advanced Industrial Science and Technology (AIST), Ikeda, Osaka 563-8577, Japan.

[d] Department of Industrial and Systems Engineering, Hong Kong Polytechnic University, Hung Hom, Kowloon, Hong Kong, P.R. China.

[e] Hong Kong Polytechnic University Shenzhen Research Institute, Shenzhen, 518057, P.R. China.

[f] National Supercomputing Center in Shenzhen, Shenzhen 518055, P.R. China.

Keywords: Lithium-Sulfur batteries; Shuttle effect; Tungsten nitride; Lithium polysulfides; Spatial confinement effect.

Abstract: To enhance the utilization of sulfur in lithium-sulfur batteries, three-dimensional tungsten nitride (WN) mesoporous foam blocks are designed to spatially localize the soluble Li_2S_6 and Li_2S_4 within the pore spaces. Meanwhile, the chemisorption behaviors of polysulfides and the capability of WN as an effective confiner are systematically investigated through density functional theoretical calculations and experimental studies. The theoretical calculations reveal a decrease chemisorption strength between WN and the soluble polysulfides (Li_2S_8 > Li_2S_6 > Li_2S_4), while the interactions between WN and the insoluble Li_2S_2/Li_2S show a high chemisorption strength of *ca*. 3 eV. Validating theoretical insights through electrochemical measurements further manifest that the assembled battery configurations with sulfur cathode confined in the thickest WN blocks deliver the best rate capabilities (1090 and 510 mAh g^{-1} at 0.5 C and 5 C, respectively) with the highest initial coulombic efficiency of 90.5 %. Moreover, a reversible capacity of 358 mAh g^{-1} is maintained with a high coulombic efficiency approaching to 100 %, even after 500 cycles at 2 C. As guided by *in silico* design, this work not only provides an effective strategy to improve the retentivity of polysulfides, but also underpins that properly architectured WN can be effective retainers of polysulfides.

1. Introduction

High-energy-density and low-cost lithium-sulfur batteries (hereafter as LSBs) have nowadays been slated amongst the most promising energy storage systems to attain the ambitious battery energy goal set at 500 Wh kg^{-1}, due to both their theoretically high gravimetric and volumetric energy density (*viz*., 2500 Wh kg^{-1} and 2800 Wh l^{-1}). [1-3] Intensive efforts have been inclined to develop high-energy, high-power, long-cycle, safe and reliable LSBs with the end-use being to power future electric vehicles and to ensure the safe, smooth and efficient operation of artificial intelligence appliances and smart grid systems. Although the theoretical energy density of LSBs are much higher than that of lithium ion batteries and sodium ion batteries, [4-6] the practical energy densities of LSBs are still limited by several scientific and technical problems. Prime among the problems faced are the intrinsically low electronic conductivity of sulfur and lithium polysulfides (hereafter as LPS), the large volume change upon cycling (up to 75 %) and the "shuttle effect" induced by the soluble long-chain LPS in organic electrolytes. [5-10] These issues apparently lead to low utilization of sulfur, rendering the poor cyclic stability and rate capability of LSBs.

To overcome the aforementioned hurdles, passionate researches have been done toward the development of advanced host structures which not only can localize the soluble LPS, but also improve the overall electronic conductivity, as summarized in **Figure 1**. [7-32] Among them, highly-conductive carbon materials with large specific surface area have been widely studied as conductive networks to improve the electronic conductivity of sulfur cathode and additionally as host structures to suppress the 'shuttle effect' induced by soluble LPS through surface physical absorption. [7-11, 33, 34] Metal compounds, such as metal oxides, [15, 24, 25] metal sulfides, [18, 35] metal nitrides (and their nanocomposites), [7, 10, 12-14, 16, 17, 25, 26] have recently been developed as

advanced hosts to further enhance the localization capability of LPS, owing to their strongly chemical absorption capability to LPS. Moreover, three-dimensional (3D) nanostructures (such as porous, hollow, hierarchical structures and their hybrid counterparts) have been revealed to show enhanced absorption capabilities by spatial localizing the soluble LPS within the 3D nanostructures. [7, 8, 11-18, 34-38] For example, hollow mesoporous TiN microsphere and tubular carbon nitride hollow spheres have been considered as one of the promising hosts for sulfur cathode to suppress the "shuttle effect" of soluble LPS during the charge/discharge process. [16, 36, 37] However, the well-designed hollow structure faces a risk of being destroyed during the rolling process of the cathode fabrication. Therefore, it is crucially important to develop a relatively dense and stable structure as advanced host for future practical LSBs.

Metal nitrides exhibit both good electrical conductivity and strong affinity for polysulfide adsorption, [7, 17] which are superior to the aforementioned compounds (*i.e.*, metal oxides, sulfides and hydroxides). Therefore, the sulfur (S) cathode hosted in titanium nitride (TiN-S) delivers a higher capacity, longer cyclic lifetime and better rate performance than S cathode hosted into TiO_2 (TiO_2-S). [16, 36] Moreover, vanadium nitride (VN)-based materials, such as conductive porous VN/graphene, Co-doped VN york-shell nanospheres entwined in carbon composite, have been developed and both achieved much superior electrochemical performance than vanadium oxide hosts. [39-42] In addition, molybdenum nitrides and tungsten nitrides have also been proposed as promising LPS reservoirs. Lately, Mosavati and co-workers' research works indicate that WN porous nanosheets exhibit stronger inhibiting effect on the "shuttle effect" of soluble LPS than both the pea-shaped VN nanoparticles and nanorod-like Mo_2N as nitride hosts. [26] In terms of resource (reserves ratio summarized in **Figure S1**, [43-46]), it is also practically attractive to conduct research relating to titanium, vanadium, molybdenum and tungsten in order to expand their

functional applications in nations such as China. Particularly for tungsten, China holds 58% of its global reserves. [46] Therefore, it is motivating to get a deeper and better understanding of the interaction behavior between WN and LPSs for developing advanced nanostructured host materials based on key elements such as tungsten.

Based on above concerns, 3D porous hierarchical WN nanobolcks (which assume a foam block architecture) were designed as relatively dense and stable reservoirs to spatially localize the soluble Li_2S_6 and Li_2S_4 within the pore space; thus obviating dissolution of LPS into the electrolyte, as explicitly illustrated in **Figure 2**. The chemical interactions between WN and various LPS species at different lithiation stages (namely, S_8, Li_2S_8, Li_2S_6, Li_2S_4, Li_2S_2 and Li_2S) are also investigated by using theoretical calculations. The calculation results indicate a decreasing sequence in the chemisorption strength between WN and the soluble Li_2S_8, Li_2S_6, Li_2S_4 polysulfides. However, worthy to note is that the interaction between WN and the insoluble LPS (*viz*., Li_2S_2 and Li_2S) recover to a level of ~3 eV. The obtained experimental results also successfully verify the theoretical insights that sulfur active cathode material hosted into WN with longer migration distance and larger confinement space exhibits superior electrochemical performance (in respect to attainable capacity, rate capability and cyclability). Overall, this work shows that a judicious design of porous hierarchical structures based on electronically-conducting metal nitrides should be helpful to promote the confinement of the soluble LPS.

2. Experimental

To validate the strategy proposed in this work, mesoporous WN nanoblocks with three different thicknesses were designed following a typical synthesis protocol shown in **Figure 2a**. Initially, WO_3 nanoblocks were prepared as precursors using a self-templating hydrothermal reaction. 3.3 g of sodium tungstate dihydrate was firstly dissolved in 50 ml of deionized water to obtain a

clear solution with a concentration of 0.2 mol L^{-1}. Subsequently, the pH value of the obtained sodium tungstate aqueous solution was adjusted to ~1 using an aqueous solution of hydrochloric acid (HCl) with a concentration of 3 mol L^{-1}. After continuous stirring for 30 min, the obtained yellow suspension was transferred and sealed into a 100 ml teflon-lined stainless steel autoclave. In order to prepare WO_3 nanoblocks with various thicknesses, the sealed autoclaves were put into electro-thermal blowing dry boxes pre-heated to 120, 140 and 160 ^oC. Following a 6-hour hydrothermal reaction, the hydrothermal products were successively washed severally with water and ethanol. Finally, the obtained WO_3 precursor products were collected and labeled as WO-120, WO-140 and WO-160, respectively, after drying at 60 ^oC for 6 hours.

WN nanoblocks were thereafter successfully prepared by nitridation of the as-prepared WO-120, WO-140 and WO-160 at 700 ^oC for 4 h in a tube furnace under ammonia (NH_3) gas atmosphere. The control experiments have been done to rationally choose the nitriding temperature for the nitridation of the as-prepared WO, see Figure S2. After cooling to room temperature, the obtained WN end products were collected and marked as WN-120, WN-140 and WN-160, respectively.

The WN-S composites were prepared via a melt-diffusion method, whereby 60 wt.% S and 40 wt.% of the as-prepared WN porous nanoblocks were ground and annealed in a tubular furnace at 155 °C for 12 h at a heating rate of 1 $^oC\ min^{-1}$. In order to get a precise content of S within the S-loaded WN foam block, thermogravimetric analysis (TG) was conducted to estimate the mass loading of S after thermal infiltration process.

The WN-S composite cathode was prepared using a mixture of 80% WN-S, 10% acetylene black, and 10% poly (vinylidene difluoride) in N, N-methylprrrolidone as solvent. CR2032 coin cells were used to assess the electrochemical performance of the as-prepared WN-S composite

cathodes. Celgard 2500 membranes and 1 M LiTFSI in 1, 2-dimethoxyethane/1, 3- dioxolane (DOL : DME = 1 : 1 by volume) with 2 % $LiNO_3$ were used as separator and electrolyte, respectively. The cells were assembled in an Ar-filled glove box with lithium foils as the counter electrodes. The average sulfur loading was about 0.92 $mg \cdot cm^{-2}$. Cycling performance tests were conducted in a Land CT2001A battery system at a voltage range of 1.7–2.8 V. Note that the capacity was based only on the mass of sulfur alone. Cyclic voltammograms were measured using a VMP3-Bio-Logic multi-channel potentiostat at a scanning rate of 0.1 mV s^{-1} in a voltage range of 1.7–2.8 V.

3. Results and discussions

3.1. Preparation of tungsten nitride (WN) and their corresponding tungsten oxide (WO_3) precursors

Hereafter we detail the preparation of mesoporous WN foam block hosts. With the aim of preparation of WO_3 nanoblocks with various thicknesses as precursors for WN synthesis, 0.2 mol L^{-1} of sodium tungstate was prepared as precursor, 3 mol L^{-1} HCl solution were used to adjust the pH value of precursor to ~ 1. The low pH value is helpful to the reaction between H^+ and WO_4^{2-} for creating large amount of $H_2WO_4 \cdot nH_2O$ seed crystal. At the beginning of the hydrothermal process, the $H_2WO_4 \cdot nH_2O$ seeds have the trend to reduce the surface energy and then gradually gathered to form two dimensional structure. [47] Then, with the increment of hydrothermal temperature and extension of duration, the two dimension structure tends to stack together. Therefore, variation in the confinement spaces (or voids) was induced through controlling the hydrothermal temperature to synthesize the WO_3 with varied thickness, as illustrated in **Figure 2a**. As shown in **Figures 3a, 3b** and **3c**, the as-prepared WO_3 nanoblocks were prepared at 120 ^oC, 140 ^oC and 160 ^oC (hereafter designated as WO-120, WO-140 and

WO-160, respectively, for brevity), adopt a cuboid morphology. Nevertheless, the thicknesses of WO-120, WO-140 and WO-160 increase from 10 ~ 40, 30 ~ 100 and 100 ~200 nm with the increase of the reaction temperature from 120 to 160 ^{o}C. X-ray diffraction (XRD) patterns furnished in **Figure 4a** indicate that the as-prepared WO_3 are unambiguously indexable in a monoclinic lattice ($P2_1/n$ space group). [44, 45]

After annealing (at 700 ^{o}C for 4 h) in a tubular furnace under ammonia gas (NH_3) atmosphere, the as-prepared WO_3 nanoblock precursors were successfully nitridized and transformed into mesoporous WN foam blocks (as shown in **Figure 2a, 3d, 3e** and **3f**). For clarity, we hereafter assign WN prepared at 120 ^{o}C, 140 ^{o}C and 160 ^{o}C as WN-120, WN-140 and WN-160, respectively. Akin to the WO-120, WO-140 and WO-160 nanoblocks, the average thicknesses of WN-120, WN-140 and WN-160 were about 40, 100, and 200 nm, respectively. The XRD patterns given in **Figure 4b** further validate the successful preparation of WN, indexable to *Pn*-3*m* cubic space group, which is consistent with the results observed from the high resolution transmission electron microscopy (HR-TEM) imaging, see **Figure S3**. The mesoporous structure is also apparent, as confirmed by the TEM image given in **Figure 3g, 3h, 3i** and the IV-type N_2 adsorption-desorption isotherm loops shown in **Figure 4c**. However, it is important to mention here that the light transmittance and Brunauer-Emmett-Teller (BET) specific surface area of the synthesized WN-120, WN-140 and WN-160 gradually decreases, due to the increase in the thickness of the nanoblocks. The calculated BET specific surface area are 51.3, 45.3 and 16.4 m^2g^{-1}, respectively, as can be seen in **Figure 4d**.

3.2. Chemisorption properties of tungsten nitride (WN) onto various Li_xS_n (x =0, 2; n =1, 2, 4, 6, 8) polysulfide species

Fundamental chemical interactions between WN and various Li_xS_n polysulfides (S_8, Li_2S_8, Li_2S_6, Li_2S_4, Li_2S_2 and Li_2S generated at different lithiation states of WN-S composite cathode) were investigated using the density functional theory (DFT) calculations. [48, 49] **Figure 5a** shows the calculated binding energy (E_b) between various Li_xS_n polysulfides and the (200) crystal plane surface of WN (WN (200)). It is evident that WN (200) shows the highest binding energy E_b of 4.01 eV toward Li_2S_8, while the calculated E_b gradually decreases to 1.44 eV when the molecular length of the soluble polysulfides decreases from Li_2S_8 to Li_2S_4. It is unprecedented that the chemical interactions between WN and insoluble LPS are recovered. The corresponding E_b between WN (200) surface and the absorbed Li_2S_2 and Li_2S are higher than 3 eV. The disparate charge densities of the adsorption systems of Li_xS_n polysulfide species on the WN (200) surface after optimization, shown in **Figure 6**, further confirms the emergence of strong chemical interactions between the Li_xS_n polysufides and the WN (200) surface in the adsorption system. The attained results further suggest that the strong chemical interactions between the Li_xS_n polysulfide species and WN emanates predominantly from interactions between sulfur (S) and tungsten (W) atoms.

To test this hypothesis, partial density of states (PDOS) calculations were performed. As shown in **Figure 5b, 5c** and **5d**, a significant overlap of virtually all the PDOS peaks appears between S-*p* and W-*d* orbitals in the energy region range of about -7.5 ~ -1 eV. Conventionally, the peak overlap indicates a strong hybridization between S-*p* and W-*d* orbital states in the adsorption system, which induces the strong S-W bonding. In contrast, the bonding effect between Li and N atoms was found to be subtle, or even ignorable. Take Li_2S_6 adsorbing on the surface as an example, **Figure 5c** displays the PDOS plots of Li-*s*, N-*s* and N-*p* orbitals. It can be clearly seen from the enlarged view that only a small peak overlap between Li-*s* and N-*p* orbitals appears in

the -5 ~ -4 eV energy region with the peak value of -4.5 eV. Therefore, it can be surmised that the strong chemisorption of WN to Li_xS_n polysulfide species is mainly dominated by the S-W bonding effects rather than the Li-N bonding. Besides, the generated S-W bond lengths (which are in the range of 2.41~2.73 Å, as listed in **Figure 6**) are also consistent with the reported S-W bond lengths (*i.e.*, 2.52 Å). [50]

To further glean on the electronic bonding effects, Bader charge differences of the generated S-W bonds after adsorption of the Li_2S_8, Li_2S_6 and Li_2S_4 polysulfide species on the WN (200) surface were calculated. The magnitude of the charge transfer between S and W was calculated to be 0.338 e, 0.234 e and 0.215 e for Li_2S_8, Li_2S_6 and Li_2S_4, respectively. As the lithiation process of sulfur (S) active cathode materials proceeds from $L_{i2}S_8$ to Li_2S_4, the charge transfer between S and W decreases, which is in accord with the trend in the variation of the binding energy of Li_xS_n polysulfide species on the WN (200) surface, as is shown in **Figure 5a**, wherein the binding energy decreases as lithiation proceeds from Li_2S_8 to Li_2S_4. In addition, the Fermi energies of the three lithiation stages were found to be -3.124, -3.082 and -2.910 eV under the condition that all energies are referenced to the vacuum level. The Fermi level shifts toward the low energy region (close to the vacuum level) as lithiation proceeds from Li_2S_8 to Li_2S_4. The downshift of Fermi level further suggests that the chemisorption of WN to the Li_xS_n polysulfides weakens from Li_2S_8 to the Li_2S_4 species, since a more energetic Fermi level is more beneficial to the stabilization of the adsorbate-surface bonds. [51] As a result, raising the energy level of the electrons facilitates an easy charge transfer between the adsorbate and the adsorbing surface, which is in agreement with the Bader charge analysis.

A preliminary conclusion can thus be drawn from theoretical calculations performed so far, that WN shows a strong adsorption ability to Li_xS_n polysulfide species and can be a promising

chemical anchor for lithium polysulfide species, in theory; thereby enhancing the energy density and cyclic stability of lithium sulfur batteries. We therefore sought to construct WN nanoblocks with a three-dimensional (3D) mesoporous hierarchical structures and controllable thickness with the aim to confine the soluble Li_xS_n within the nanoscale local space and to prevent the loss of active Li_xS_n polysulfides from WN-hosted sulfur cathode into the electrolyte.

3.3. Electrochemical performance of sulfur confine in the tungsten nitride (WN) foam block hosts

To verify the proposed concept of confining the soluble by increasing the local space within the as-prepared WN nanoblocks, WN-S composite cathodes (containing 60 *wt*.% of sulfur (S) and 40 *wt*.% of WN porous nanoblocks) were prepared via a physical mixing method, followed by a melt-diffusion infiltration process. The large surface area and the porous structure could provide large surface and space to accommodate active S materials. After the thermal infiltration process, the calculated S-loading within S/WN-160 composite still remain ~ 59 wt% based on the TG analysis results shown in **Figure S4**. **Figure S5** shows the TEM images of WN-S composite cathode and the corresponding elemental mapping of W, N and S. The transmission electron microscopy (TEM) images shown in **Figure S5a** indicate that the mesoporous structure is maintained after the infiltration of S. Additionally, the infiltrated S active materials were uniformly distributed and contained element W and N without gathering into the bulk S (see **Figures S5b**, **S5c**, **S5d**, **S5e** and **S5f**). The electrochemical performance of the assembled lithium sulfur batteries comprising the synthesized WN-120/S, WN-140/S and WN-160/S composites as cathode materials are presented in **Figures 7**, **S6, S7** and **S8**. Typical (dis)charge voltage profiles of the lithium sulfur batteries assembled with the composite cathodes consisting of WN-120/S, WN-140/S and WN-160/S, cycled at a current density equivalent to 0.5 C rate, are furnished in

Figure 7a. WN-160/S exhibits much higher discharge and charge capacity, which is respectively 228 and 332 mAh g^{-1} higher than those of WN-140/S. This indicates that more soluble lithium polysulfides (LPS) have dissolved into the electrolyte, while less have transformed into stable Li_2S. Moreover, WN-160/S shows much higher initial coulombic efficiency (90.3%) than WN-140/S (77.3%) and WN-120/S (79%). Note here that, the attained results imply that WN-160 shows higher retentivity of soluble LPS than WN-140 and WN-120, presumably emanating from the enhanced spatial confinement effect imparted by the thickness' increase. Additional experiments have been done to check the electrochemical performance of WN anode materials within the electrolyte for Li-S batteries. The charge/discharge profiles were present in **Figure S6**. From **Figures S6a** and **S6b**, it can be seen that the capacity of neat WN host without S cathode materials is lower than 10 mAh g^{-1}, and keep stable during the 200 cycles. Therefore, we think the capacity contribution to the S/WN composite cathode materials could be ignored. **Figures 7b** and **S7** indicate that the as-synthesized WN mesoporous nanoblock hosts deliver good rate capability and cyclic stability, which are comparable to other reported metal nitride hosts. Typical cyclic voltammetry (CV) curves and electrochemical impedance spectroscopy (EIS) profiles shown in **Figure S8** are in line with the reported trend. [16, 25] The CV curves and EIS profiles reveal improved electrochemical activity and reduced charge transfer resistance as well as cyclic stability of WN-160/S cathode in comparison to others. WN-160/S composite cathode delivers charge capacities of 1090, 909, 788 and 510 mAh g^{-1} at a current density of 0.5 C, 1 C, 2 C and 5 C, respectively. After 20 cycles, the charge capacity recovers to 950 mAh g^{-1} when the applied current density is set back to 0.5 C. In summary, WN-160/S composite cathode presents excellent rate capability and cyclic performance, as seen in **Figures 7c and 7d**. The charge capacity could still be retained at 631.4, 578.2 and 414.1 mAh g^{-1} after cycling at 1 C, 2 C and 5

C rate for 200 cycles, respectively. Even after 500 cycles at a current density commensurate to 2 C rate, the capacity is maintained at 358 mAh g^{-1} with a stable coulombic efficiency close to 100%, as apparent in **Figure 7c**. The TEM image of the cycled S/WN composite cathode materials provided in **Figure S9** further confirm that no obvious structure change is observed after 200 cycles, and the porous block structure still maintains.

At this juncture, it is important to also investigate the chemisorption ability of the as-prepared mesoporous WN foam blocks. To do so, equivalent amounts of acetylene black (AB), WN-120, WN-140 and WN-160 were added into a blank solution of Li_2S_x in tetrahydrofuran. It is interesting to note that the brown solution of Li_2S_x in tetrahydrofuran fades to a colorless solution after stirring for 4 h at room temperature. The optical images shown in **Figure S10** further manifest that the increase of the confinement space with cubic thickness of WN can effectively promote the absorption capability to Li_2S_x polysulfides. To further garner information relating to the adsorption mechanism of the mesoporous WN foam blocks, Li_2S_6 solution was measured by UV/Vis absorption. **Figure S10** shows the obtained UV/Vis adsorption spectra. A conspicuously wide absorption shoulder peak ranging from about 230 to 350 nm, which corresponds to the S_4^{2-} /S_6^{2-}/S_8^{2-} species, can be clearly observed from the blank Li_2S_x solution. The intensity of the spectrum of the AB-added solution is slightly lower than that of the blank Li_2S_x solution, indicating that AB has a relatively weak adsorption capability for Li_2S_x. As for the solution containing WN in contrast, the absorption peak in UV/Vis adsorption spectra of Li_2S_x solution are much lower than the blank Li_2S_x solution and decrease with the increase of the cubic thickness of WN. This further implies a strong chemisorption ability of the as-prepared WN and the confinement effect increase with the increase in the cubic thickness of WN.

To our surprise, the aforementioned experimental results are consistent with the theoretical calculations shown in **Figure 5a**. The as-prepared WN exhibits an enhanced confinement effect to Li_2S_x upon increase of the cubic thickness, which implies an increase in the diffusion distance and time for soluble Li_2S_6 and Li_2S_4 (which are generated during the (dis)charge process of WN/S composite cathode) to migrate from inner to outer surfaces of WN nanoblocks. To benchmark the performance of the architectured WN foam blocks delved in this study, a comparison of the electrochemical performance of WN-160/S composite cathode (which exhibits the best performance) with other recently reported counterpart cathodes with similar active loading of about 1 $mgcm^{-2}$ was done. **Figure 7e** shows a comparative plot of WN-160/S along with other host nitrides.[10, 14, 25, 36, 42] Mesoporous WN nanoblocks that adopt a "foam block" architecture, that we report in this study, exhibits comparable and even better performance than other metal nitride counterparts, although the calculated binding energy (E_b = 2.26 eV) of the Li_2S_6 on the WN surface is lower than the reported binding energy of 3.75 eV for the Li_2S_6 on the (200) surface of VN. [7] Therefore, we believe that the large confinement space conferred from the mesoporous structure of the thick WN adsorbent has a profound effect on impeding the dissolution of Li_2S_x polysulfide species into the electrolyte. Thus, contributing to the improvement of utilization and cycle life of sulfur active cathode materials, while rendering WN as an effective retainer or confiner of Li_2S_x, as demonstrated in **Figure 2b**. Ample room for the further advancement of the present work still exists. Some critical issues emerge to be solved prior to using tungsten nitride (WN) as host structures for sulfur active cathode materials, albeit the calculated binding energy between WN and Li_xS_n species are comparable to other nitride counterparts, but higher than some of the metal oxide, sulfides and halides studied in references 7 and 52 (as presented in **Figure 5a**). Considerations that warrant to be addressed are strategies

to avert the loss of soluble LPS from the surface of WN nanoparticles, particularly at various (dis)charging states of Li_2S_4, since the binding energy decreases drastically with the variation of the (dis)charging states from Li_2S_8 to Li_2S_4. This certainly calls for further nanoscale spatial localization strategies of sulfur into tungsten nitride and related electronically-conducting nitrides aided by computational approaches.

4. Conclusion

The capability of tungsten nitride (WN) as a favorable host structure to confine sulfur, as an active cathode material for lithium-sulfur batteries, has been investigated experimentally augmenting atomistic theoretical calculations. Theoretical calculations reveal a decreasing sequence in the chemisorption strength between WN and soluble LPS (namely, Li_2S_8 > Li_2S_6 > Li_2S_4), while interactions with insoluble polysulfides such as Li_2S_2 and Li_2S recover to an unprecedented level of ~3 eV. Based on the theoretical insights, three-dimensional nanostructured mesoporous WN foam blocks were designed to spatially localize the soluble polysulfides within the pore space; thus circumventing polysulfide dissolution into the electrolyte. Lithium sulfur batteries assembled using sulfur encapsulated in the electronically-conducting and nano-architectured WN (as a composite cathode) delivers excellent rate capability and cyclic performance. Noteworthy are charge capacities of 1090, 909, 788 and 510 mAh g^{-1} at a current density commensurate to 0.5 C, 1 C, 2 C and 5 C rate, respectively, and stable coulombic efficiency approaching 100 % upon cycling at 2 C rate for 500 cycles. Altogether, this work reveals that properly architectured metal nitrides (such as the electronically conducting tungsten nitride (WN)) can be effective confiners of soluble polysulfides, thus advancing the development of high-energy-density and long-life lithium-sulfur batteries.

ASSOCIATED CONTENT

Supporting Information

Figure S8. Cyclic voltammograms at (a) the second and (b) fifth cycles of the composite cathodes of WN-120/S, WN-140/S and WN-160/S at a scanning rate of 0.1 mV s^{-1}, (c) The EIS of WN at the initial state and (d) after fifth CV cycles of the electrode of WN-120/S, WN-140/S and WN-160/S at a scanning rate of 0.1 mV s^{-1}.

Figure S9. The TEM image of WN-160 nanoblock after 200 cycles.

Figure S10. UV/Vis adsoption spectra of Li_2S_6 tetrahydrofuran solutions after addition of acetylene black, WN-120, WN-140 and WN-160 for 4 h. Inset shows the optical images.

AUTHOR INFORMATION

‡ *Dr. Zhen-Dong Huang and Mr. Yanwu Fang contributed equally to this work.*

Corresponding Author

* E-mail address: wuz2015@mail.xjtu.edu.cn (Z. Wu);

titus.masese@aist.go.jp (T. Masese);

iamywma@njupt.edu.cn. (Y. W. Ma)

Notes

The authors declare no competing financial interest.

Acknowledgements

This work was conducted under the auspices of the National Natural Science Foundation of China (51772157, 21805140, 21736008, Natural Science Foundation of Jiangsu Province (BK20181396), Natural Science Foundation of the Higher Education Institutions of Jiangsu

Province (18KJB430020), Priority Academic Program Development of Jiangsu Higher Education Institutions (PAPD) (YX03002), Jiangsu National Synergistic Innovation Center for Advanced Materials (SICAM), Natural Science Foundation of Shaanxi Province (2017JQ5059), Foundation of NJUPT (NY217077) and PolyU Start-up Fund for New Recruits (No. 1-ZE8R).

References

1) Zou, P. C.; Wang, Y.; Chiang, S. W.; Wang, X. Y.; Kang, F. Y.; Yang, C. Directing Lateral Growth of Lithium Dendrites in Micro-Compartmented Anode Arrays for Safe Lithium Metal Batteries. *Nat. Commun.* **2018,** *9*, 464.

(2) Zhang, W. D.; Tu, Z. Y.; Qian, J. W.; Choudhury, S.; Archer L. A.; Lu, Y. Y. Design Principles of Functional Polymer Separators for High-Energy, Metal-Based Batteries. *Small* **2018,** *14*, 1703001.

(3) Pang, Q.; Kundu D.; Nazar, L. F. A Graphene-like Metallic Cathode Host For Long-Life and High-Loading Lithium-Sulfur Batteries. *Mater. Horiz.* **2016,** *3*, 130—136.

(4) Luo, B.; Hu, Y. X.; Zhu, X. B.; Qiu, T. F.; Zhi, L. J.; Mu Xiao, Zhang, H. J.; Zou, M. C.; Cao, A. Y.; Wang, L. Z. Controllable Growth of SnS_2 Nanostructures on Nanocarbon Surfaces for Lithium-Ion and Sodium-Ion Storage with High Rate Capability. *J. Mater. Chem. A*, **2018**, *6*, 1462—1472.

(5) Xia, S. S.; Wang, Y. R. Liu, Y.; Wu, C. H.; Wu, M. H.; Zhang. H. J. Ultrathin MoS_2 Nanosheets Tightly Anchoring onto Nitrogen-Doped Graphene for Enhanced Lithium Storage Properties. *Chem. Eng. J.,* **2018**, *332*, 431-439.

(6) Lei, Z. D.; Xu, L. Q.; Jiao, Y. L.; Du, A. J.; Zhang, Y.; Zhang. H. J. Strong Coupling of MoS_2 Nanosheets and Nitrogen-Doped Graphene for High-Performance Pseudocapacitance Lithium Storage. *Small* **2018,** *14*, 1704410.

(7) Sun, Z. H.; Zhang, J. Q.; Yin, L. C.; Hu, G. J.; Fang, R. P.; Cheng, H. M.; Li, F. Conductive Porous Vanadium Nitride/Graphene Composite as Chemical Anchor of Polysulfides for Lithium-Sulfur Batteries. *Nat. Commun.* **2017,** *8*, 14627.

(8) Wu, H. L.; Xia, L.; Ren, J.; Zheng, Q. J.; Xu, C. G.; Lin, D. M. A High-Efficiency N/P Co-Doped Graphene/CNT@porous Carbon Hybrid Matrix as a Cathode Host for High Performance Lithium–Sulfur Batteries. *J. Mater. Chem. A* **2017,** *5*, 20458—20472.

(9) Yang, W.; Yang, W.; Song, A. L.; Sun, G.; Shao, G. J. 3D Interconnected Porous Carbon Nanosheets/Carbon Nanotubes as a Polysulfide Reservoir for High Performance Lithium–Sulfur Batteries. *Nanoscale* **2018,** *10*, 816—824.

(10) Zhang, J.; You, C. Y.; Zhang, W. H.; Wang, J.; Guo, S. H.; Yang, R.; Xu, Y. H. Conductive Bridging Effect of TiN Nanoparticles on the Electrochemical Performance of TiN@CNT-S Composite Cathode. *Electrochim. Acta* **2017,** *250*, 159—166.

(11) Wu, F.; Qian, J.; Wu, W. P.; Ye, Y. S.; Sun, Z. G.; Xu, B.; Yang, X. G.; Xu, Y. H.; Zhang, J. T.; Chen, R. J. Boron-Doped Microporous Nano Carbon as Cathode Material for High-Performance Li-S Batteries. *Nano Res.* **2017,** *10*, 426—436.

(12) Li, X. L.; Tang, R. W.; Hu, K.; Zhang, L. Y.; Ding, Z. Q. Hierarchical Porous Carbon Aerogels with VN Modification as Cathode Matrix for High Performance Lithium-Sulfur Batteries. *Electrochim. Acta* **2016,** *210*, 734—742.

(13) Jiang, G. S.; Xu, F.; Yang, S. H.; Wu, J. P.; Wei, B. Q.; Wang, H. Q. Mesoporous, Conductive Molybdenum Nitride as Efficient Sulfur Hosts for High-Performance Lithium-Sulfur Batteries. *J. Power Sources* **2018,** *395*, 77—84.

(14) Cui, Z. M.; Zu, C. X.; Zhou, W. D.; Manthiram, A.; Goodenough, J. B. Mesoporous Titanium Nitride-Enabled Highly Stable Lithium-Sulfur Batteries, *Adv. Mater.* **2016,** *28*, 6926—6931.

(15) Ma, F.; Liang, J. S.; Wang, T. Y.; Chen, X.; Fan, Y. N.; Hultman, B.; Xie, H.; Han, J. T.; Wu, G.; Li, Q. Efficient Entrapment and Catalytic Conversion of Lithium Polysulfides on Hollow Metal Oxides Submicro-Spheres as Lithium-Sulfur Battery Cathodes. *Nanoscale* **2018,** *10*, 5634—5641.

(16) Deng, D. R.; An, T. H.; Li, Y. J.; Wu, Q. H.; Zheng, M. S.; Dong, Q. F. Hollow Porous Titanium Nitride Tubes as Cathode Electrode for Extremely Stable Li-S Battery. *J. Mater. Chem. A* **2016,** *4*, 16184—16190.

(17) Zhou, T. H.; Lv, W.; Li, J.; Zhou, G. M.; Zhao, Y.; Fan, S. J.; Liu, B. L.; Li, B. H.; Kang, F. Y.; Yang, Q. H. Twin Born TiO_2–TiN Heterostructures Enabling Smooth Trapping–Diffusion–Conversion of Polysulfides towards Ultralong Life Lithium–Sulfur Batteries. *Energy Environ. Sci.* **2017,** *10*, 1694—1703.

(18) Cheng, Z. B.; Xiao, Z. B.; Pan, H.; Wang, S. Q.; Wang, R. H. Elastic Sandwich-Type rGO–VS_2/S Composites with High Tap Density: Structural and Chemical Cooperativity Enabling Lithium–Sulfur Batteries with High Energy Density. *Adv. Energy Mater.* **2018,** *8*, 1702337.

(19) Cheng, Z. B.; Pan, H.; Zhong, H.; Xiao, Z. B.; Li, X. J.; Wang, R. H. Porous Organic Polymers for Polysulfide Trapping in Lithium-Sulfur Batteries. *Adv. Funct. Mater.* **2018,** *28*, 1707597.

(20) Jia, P.; Hu, T. D.; He, Q. B.; Cao, X.; Ma, J. P.; Fan, J. B.; Chen, Q.; Ding, Y. H.; Pyun, J.; Geng, J. X. Synthesis of Macroporous Conjugated Polymer Framework: Iron Doping for Highly Stable, Highly Efficient Lithium-Sulfur Batteries. *ACS Appl. Mater. Interfaces* **2019,** *11*, 3087-3097.

(21) Zhou, J. W.; Yu, X. S.; Fan, X. X.; Wang, X. J.; Li, H. W.; Zhang, Y. Y.; Li, W.; Zheng, J.; Wang, B.; Li, X. G. The Impact of the Particle Size of a Metal-Organic Framework for Sulfur Storage in Li-S Batteries. *J. Mater. Chem. A* **2015,***3*, 8272—8275.

(22) Bai, S. Y.; Liu, X. Z.; Zhu, K.; Wu, S. C.; Zhou, H. S. Metal–Organic Framework-Based Separator for Lithium–Sulfur Batteries. *Nat. Energy* **2016,** *1*, 16094.

(23) Liang, X.; Kwok, C. Y.; Lodi-Marzano, F.; Pang, Q.; Cuisinier, M.; Huang, H.; Hart, C. J.; Houtarde, D.; Kaup, K.; Sommer, H.; Brezesinski, T.; Janek, J.; Nazar, L. F. Tuning Transition Metal Oxide–Sulfur Interactions for Long Life Lithium Sulfur Batteries: The "Goldilocks" Principle. *Adv. Energy Mater.* **2016,** *6*, 1501636.

(24) He, J. R.; Luo, L.; Chen, Y. F.; Manthiram, A. Yolk–Shelled C@Fe_3O_4 Nanoboxes as Efficient Sulfur Hosts for High-Performance Lithium–Sulfur Batteries. *Adv. Mater.* **2017,** *29*, 1702707.

(25) Hao, Z. X.; Yuan, L. X.; Chen, C. J.; Xiang, J. W.; Li, Y. Y.; Huang, Z. M.; Hu, P.; Huang, Y. H. TiN as a Simple and Efficient Polysulfide Immobilizer for Lithium–Sulfur Batteries. *J. Mater. Chem. A* **2016,** *4*, 17711—17717.

(26) Mosavati, N.; Salley, S. O.; Ng, K. Y. S. Characterization and Electrochemical Activities of Nanostructured Transition Metal Nitrides as Cathode Materials for Lithium Sulfur Batteries. *J. Power Sources* **2017,** *340*, 210—216.

(27) Li, X. X.; Gao, B.; Huang, X.; Guo, Z. J.; Li, Q. W.; Zhang, X. M..; Chu, P. K. and Huo, K. F. Conductive Mesoporous Niobium Nitride Microspheres/Nitrogen-Doped Graphene Hybrid with Efficient Polysulfide Anchoring and Catalytic Conversion for High-Performance Lithium–Sulfur Batteries. *ACS Appl. Mater. Interfaces* **2019**, *11*, 2961-2969.

(28) Gao, B.; Li, X. X.; Ding, K.; Huang, C.; Li, Q. W.; Chu, P. K.; and Huo, K. F. Recent Progress in Nanostructured Transition Metal Nitrides for Advanced Electrochemical Energy Storage. *J. Mater. Chem. A* **2019**, *7*, 14-37.

(29) Xin, S.; Gu, L.; Zhao, N. H.; Yin, Y. X.; Zhou, L. J.; Guo, Y. G.; and Wan, L. J. Smaller Sulfur Molecules Promise Better Lithium−Sulfur Batteries. *J. Am. Chem. Soc.* **2012**, *134,* 18510−18513.

(30) Xin, S.; Yin, Y. X.; Wan, L. J.; and Guo, Y. G. Encapsulation of Sulfur in a Hollow Porous Carbon Substrate for Superior Li-S Batteries with Long Lifespan. *Part. Part. Syst. Charact*. **2013,** *30*, 321–325.

(31) Xin, S.; You, Y.; Lin, H. Q.; Zhou W. D.; Li, Y. T.; Xue, L. G.; and Cong H. P Graphene Sandwiched by Sulfur-Confined Mesoporous Carbon Nanosheets: A Kinetically Stable Cathode for Li−S Batteries. *ACS Appl. Mater. Interfaces* **2016**, *8*, 33704−33711

(32) Chen, Z. H.; Du, X. L.; He, J. B.; Li, F.; Wang, Y.; Li, Y. L; Li, B.; and Xin, S. Porous Coconut Shell Carbon Offering High Retention and Deep Lithiation of Sulfur for Lithium−Sulfur Batteries. *ACS Appl. Mater. Interfaces* **2017**, *9*, 33855−33862.

(33) Yao, W. Q.; Chu, C. J.; Zheng, W. Z.; Zhan, L.; Wang, Y. L. "Pea-pod-like" Nitrogen-Doped Hollow Porous Carbon Cathode Hosts Decorated with Polar Titanium Dioxide Nanocrystals as Efficient Polysulfide Reservoirs for Advanced Lithium–Sulfur Batteries. *J. Mater. Chem. A* **2018,** *6*, 18191—18205.

(34) Yang, C. P.; Yin, Y. X.; Ye, H.; Jiang, K. C.; Zhang, J.; Guo, Y. G. Insight into the Effect of Boron Doping on Sulfur/Carbon Cathode in Lithium–Sulfur Batteries. *ACS Appl. Mater. Interfaces* **2014,** *6*, 8789—8795.

(35) Lin, H. B.; Yang, L. Q.; Jiang, X.; Li, G. C.; Zhang, T. R.; Yao, Q. F.; Zheng, G. W.; Lee, J. Y. Electrocatalysis of Polysulfide Conversion by Sulfur-Deficient MoS_2 Nanoflakes for Lithium–Sulfur Batteries. *Energy Environ. Sci.* **2017,** *10*, 1476—1486.

(36) Chen, L.; Yang, W. W.; Zhang, H.; Liu, J. G.; Zhou, Y. Self-Templated Preparation of Hollow Mesoporous TiN Microspheres as Sulfur Host Materials for Advanced Lithium–Sulfur Batteries. *J. Mater. Sci.* **2018,** *53*, 10363—10371.

(37) Meng, Z.; Li, S. J.; Ying, H. J.; Xu, X.; Zhu, X. L.; Han, W. Q. From Silica Sphere to Hollow Carbon Nitride - Based Sphere: Rational Design of Sulfur Host with Both Chemisorption and Physical Confinement. *Adv. Mater. Interfaces* **2017,** *4*, 1601195.

(38) Li, Z.; Zhang, J. T.; Guan, B. Y.; Lou, X. W. Mesoporous Carbon@Titanium Nitride Hollow Spheres as an Efficient SeS_2 Host for Advanced Li–SeS2 Batteries. *Angew. Chem. Int. Ed.* **2017,** *56*, 16003—16007.

(39) Ma, L. B.; Yuan, H.; Zhang, W. J.; Zhu, G. Y.; Wang, Y. R.; Hu, Y.; Zhao, P. Y.; Chen, R. P.; Chen, T.; Liu, J.; Hu, Z.; Jin, Z. Porous-Shell Vanadium Nitride Nanobubbles with Ultrahigh Areal Sulfur Loading for High-Capacity and Long-Life Lithium−Sulfur Batteries. *Nano Lett.* **2017,** *17*, 7839—7846.

(40) Li, X. X.; Ding, K.; Gao, B.; Li, Q. W.; Li, Y. Y.; Fu, J. J.; Zhang, X. M.; Chu, P. K.; Huo, K. F. Freestanding Carbon Encapsulated Mesoporous Vanadium Nitride Nanowires Enable Highly Stable Sulfur Cathodes for Lithium-Sulfur Batteries. *Nano Energy* **2017,** *40*, 655—662.

(41) Zhong, Y.; Chao, D. L.; Deng, S. J.; Zhan, J. Y.; Fang, R. Y.; Xia, Y.; Wang, Y. D.; Wang, X. L.; Xia, X. H.; Tu, J. P. Confining Sulfur in Integrated Composite Scaffold with Highly Porous Carbon Fibers/Vanadium Nitride Arrays for High-Performance Lithium–Sulfur Batteries. *Adv. Funct. Mater.* **2018,** *28*, 1706391.

(42) Ren, W. J.; Xu, L. Q.; Zhu, L.; Wang, X. Y.; Ma, X. J.; Wang, D. B. Cobalt-Doped Vanadium Nitride Yolk–Shell Nanospheres @ Carbon with Physical and Chemical Synergistic Effects for Advanced Li–S Batteries. *ACS Appl. Mater. Interfaces* **2018,** *10*, 11642—11651.

(43) Titanium resource reserves, distribution and mineral production, Metal Encyclopedia, http://baike.asianmetal.cn/metal/ti/resources&production.shtml.

(44) Vanadium resource reserves and mineral production, Metal Encyclopedia, http://baike.asianmetal.cn/metal/V/resources&production.shtml.

(45) Molybdenum resource reserves distribution and production, Metal Encyclopedia, http://baike.asianmetal.cn/metal/mo/resources&production.shtml.

(46) Tungsten resource distribution and production, Metal Encyclopedia, http://baike.asianmetal.cn/metal/w/resources&production.shtml.

(47) Yin, M. L.; Yu, L. M.; Liu, S. Z. Synthesis of Thickness-Controlled Cuboid WO3 Nanosheets and their Exposed Facets Dependent Acetone Sensing Properties. *J. Alloys and Compounds* **2017**, *696*, 490-497.

(48) Kresse, G.; Hafner, J. Ab initio Molecular Dynamics for Liquid Metals. *Phys. Rev. B* **1993,** *47*, 558-561.

(49) Kresse, G.; Furthmüller, J. Efficiency of Ab-initio Total Energy Calculations for Metals and Semiconductors Using a Plane-Wave Basis Set. *Comput. Mater. Sci.* **1996,** *6*, 15—50.

(50) Adams, R. D.; Babin, J. E.; Natarajan, K.; Tasi, M.; Wang, J. G. Cluster Synthesis. 15. Square-Pyramidal Coordination of Sulfur in Metal Cluster Complexes. Synthesis and Structural Characterizations of $Ru_4(CO)_7$(.mu.-$CO)_2(PMe_2Ph)_2$(.mu.4-S)(.mu.5-S)[$W(CO)_4PMe_2Ph$] and $Os_5(CO)_{15}$(.mu.5-S)[$W(CO)_4PPh_3$]. *Inorg. Chem.* **1987,** *26*, 3708—3713.

(51) Akbashev, A. R.; Zhang, L.; Mefford, J. T.; Park, J.; Butz, B.; Luftman, H.; Chueh, W. C.; Vojvodic, A. Activation of Ultrathin $SrTiO_3$ with Subsurface $SrRuO_3$ for the Oxygen Evolution Reaction. *Energy Environ. Sci.* **2018,** *11*, 1762—1769.

(52) Zhang, Q. F.; Wang, Y. P.; Seh, Z. W.; Fu, Z. H.; Zhang, R. F.; Cui, Y. Understanding the Anchoring Effect of Two-Dimensional Layered Materials for Lithium-Sulfur Batteries. *Nano Letters* **2015,** *15*, 3780—3786.

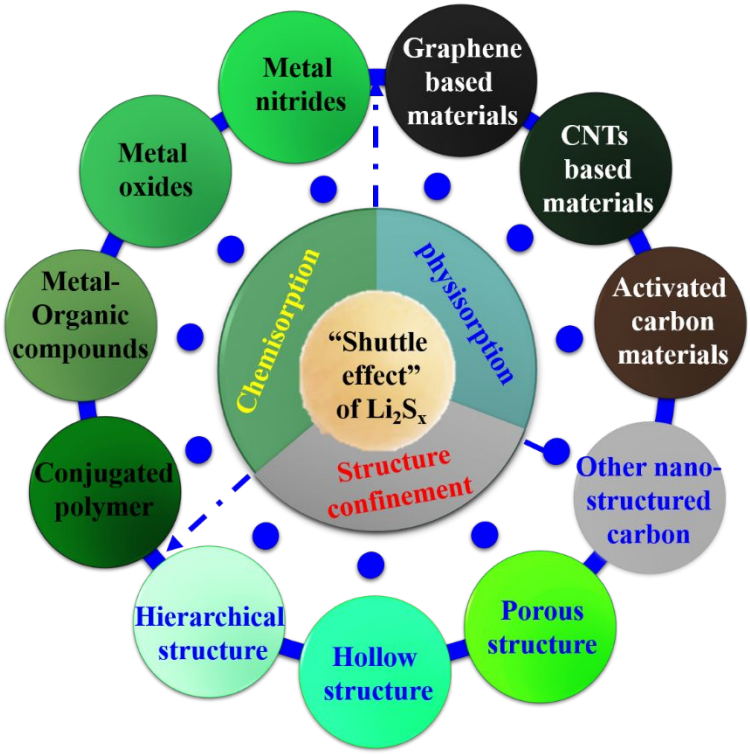

Figure 1. The reported main hosts and reservoir of sulfur and lithium polysulfides along with their working mechanisms. [7-32]

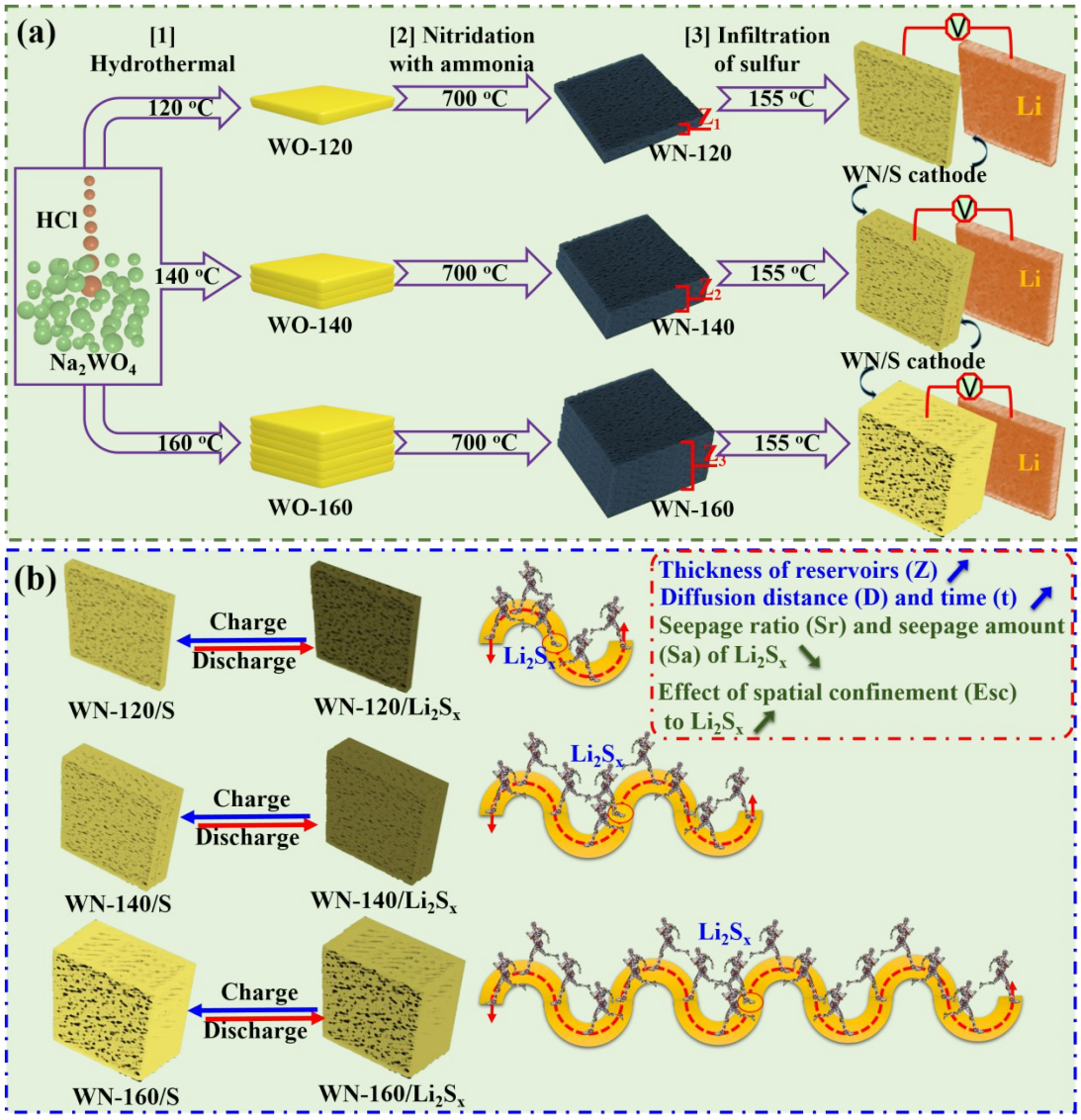

Figure 2. Schematic of (a) the typical synthesis protocol of mesoporous tungsten nitride (WN) with controllable thickness and (b) their distinct spatial confinement effect which induces the strong polysulfides retentivity of the mesoporous tungsten nitride foam blocks.

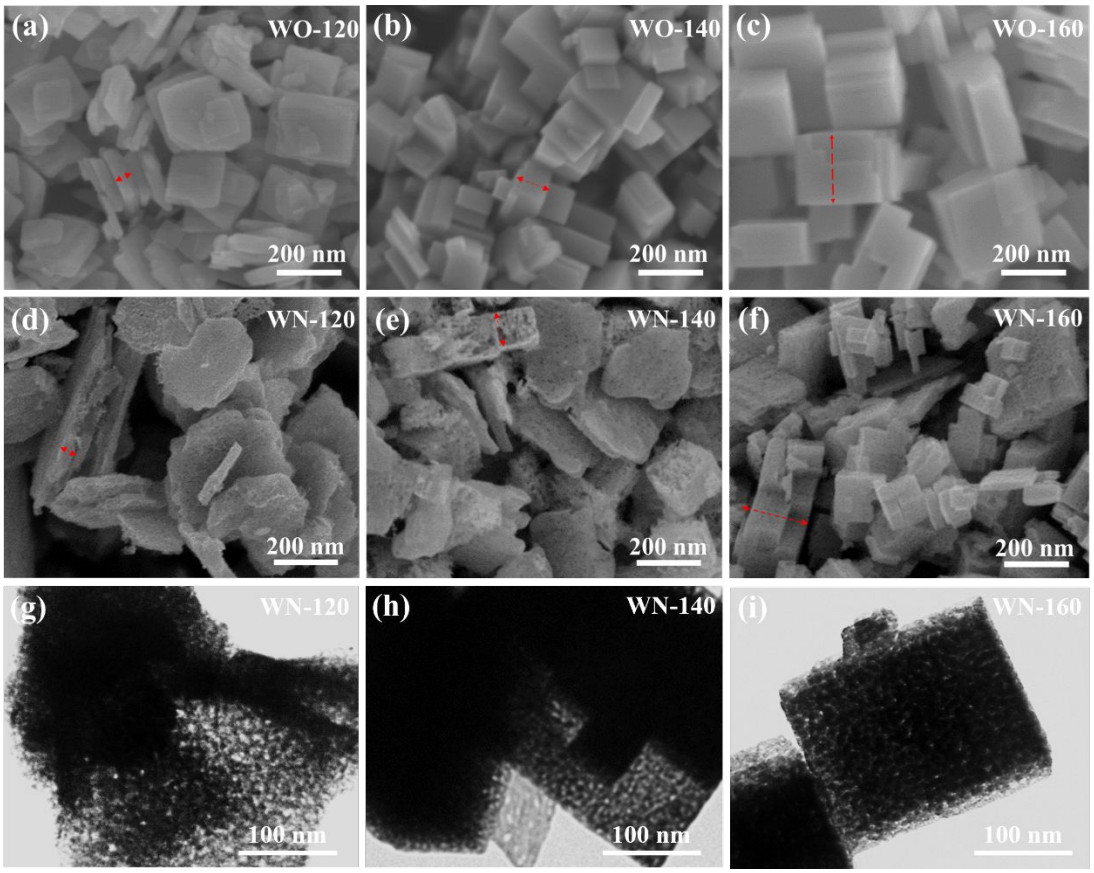

Figure 3. Scanning electron microscopy (SEM) images of tungsten oxide (WO_3) precursors prepared at (a) 120 ^oC, (b) 140 ^oC and (c) 160 ^oC (hereafter denoted as WO-120, WO-140 and WO-160, respectively, for clarity's sake). SEM images (d, e, f) and TEM images (g, h, i) of tungsten nitride (WN) end products prepared using the WO_3 precursors of WO-120, WO-140 and WO-160 (labeled as WN-120, WN-140 and WN-160, respectively).

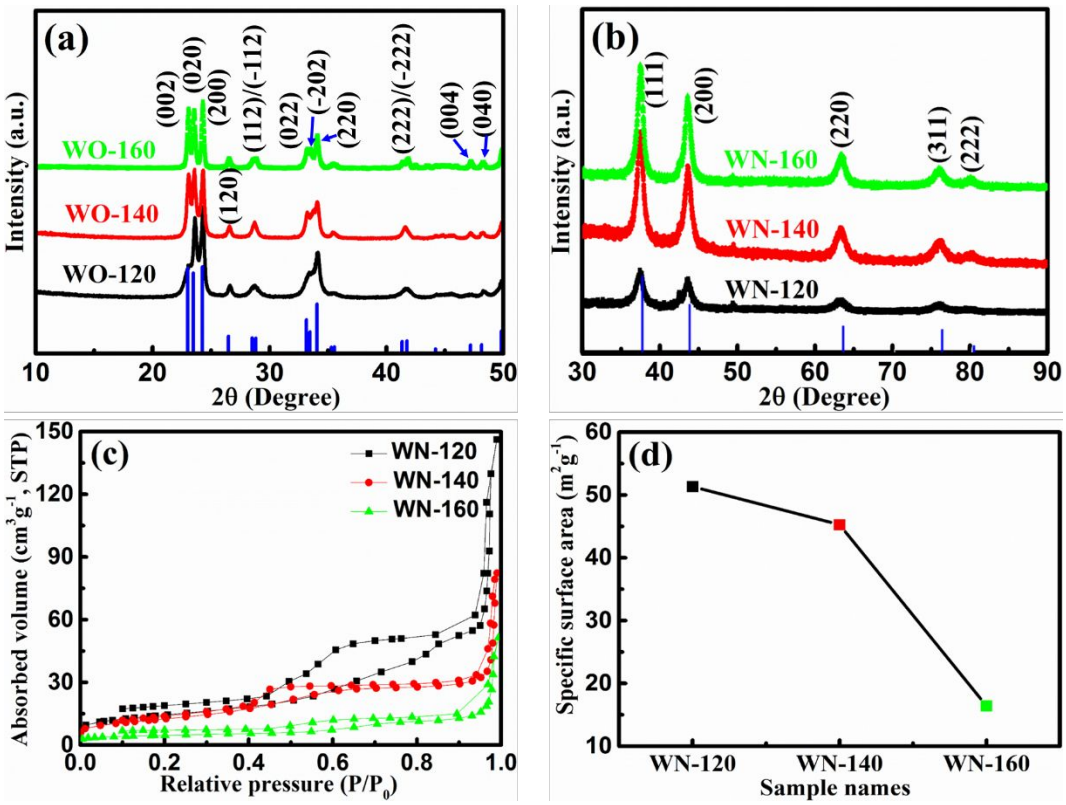

Figure 4. (a) X-ray diffraction (XRD) patterns of WO_3 precursors (WO-120, WO-140 and WO-160), (b) XRD patterns of as-prepared WN (WN-120, WN-140 and WN-160), (c) Nitrogen gas (N_2) adsorption-desorption isotherm loops of the as-prepared WN and (d) the Brunauer–Emmett–Teller (BET) specific surface area for the as-prepared WN.

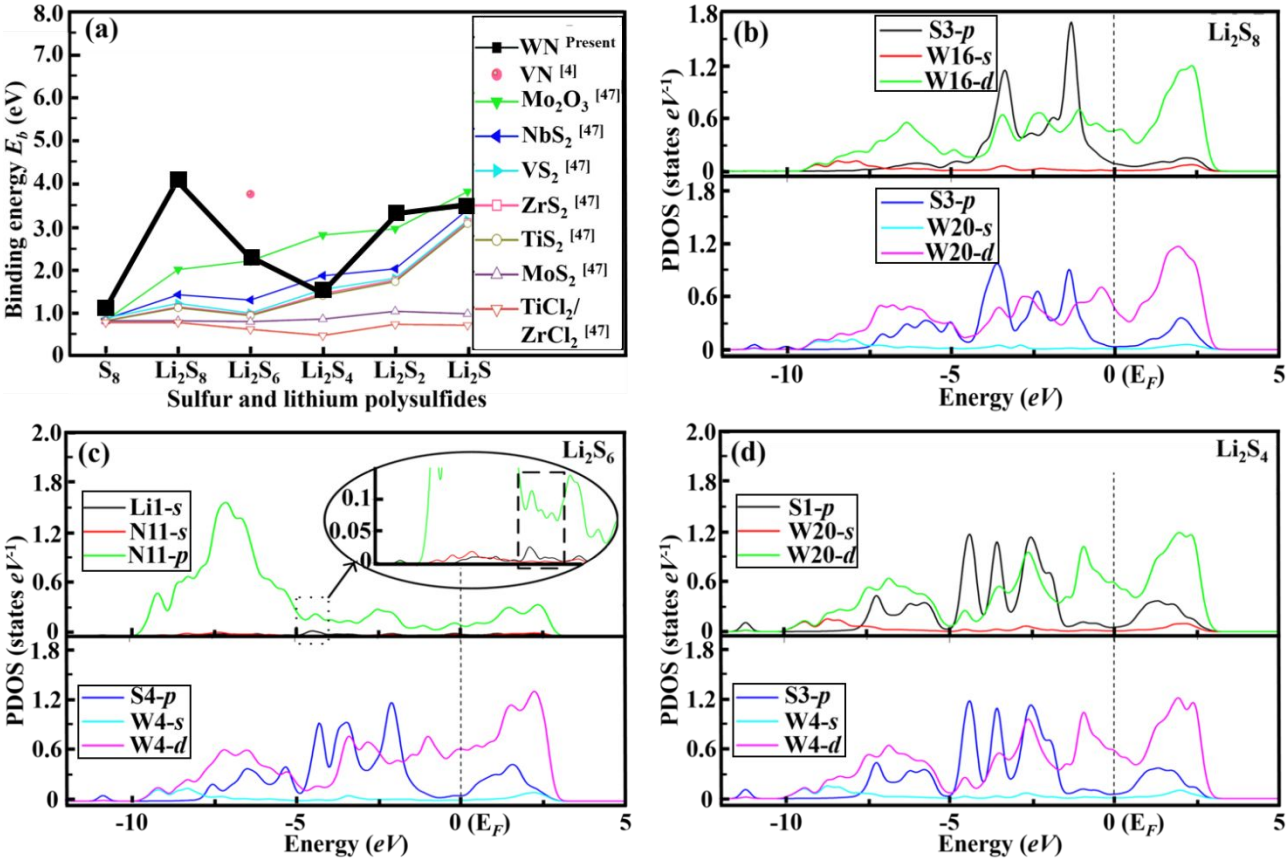

Figure 5. (a) Binding energies for the Li_xS_n species at different lithiation stages on the (200) adsorbing surface of tungsten nitride (WN) and partial density of states (PDOS) of the polysulfides on the (200) adsorbing surface of WN: (b) Li_2S_8, (c) Li_2S_6, and (d) Li_2S_4. (Note that the italicized arabic numerals after S3, S4, Li1, N11 W4, W16 and W20 denote the atomic sequence number within the applied structure model.)

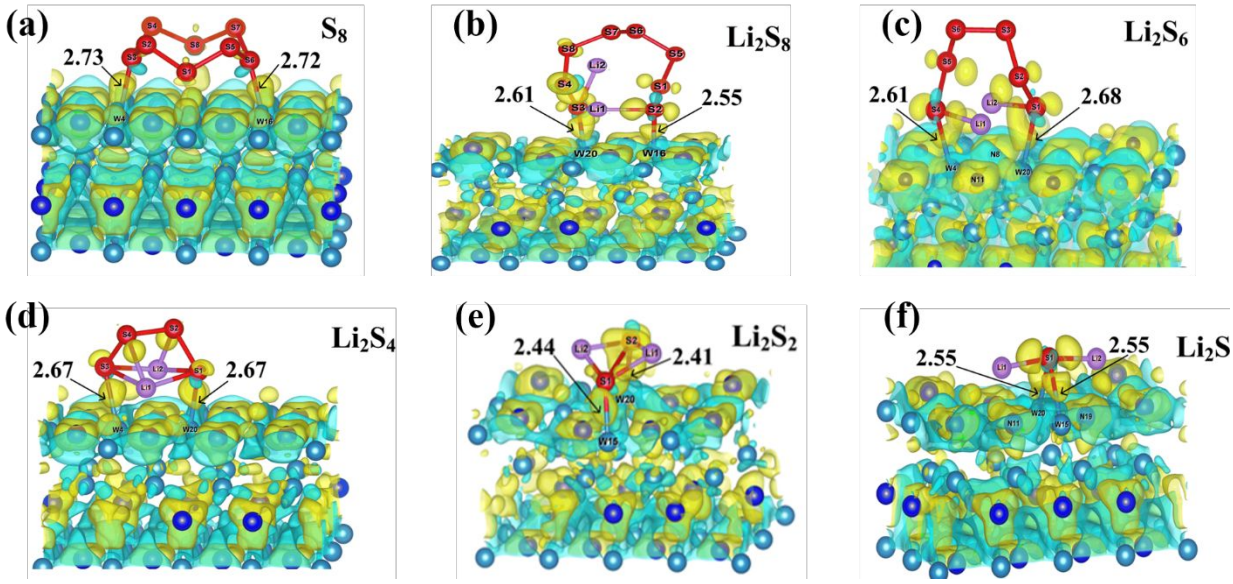

Figure 6. Calculated charge densities of Li_xS_n (x = 0, 2; n = 1, 4, 6, 8) polysulfide species on the (200) adsorption surface of tungsten nitride (WN) after geometry optimization: (a) S, (b) Li_2S_8, (c) Li_2S_6, (d) Li_2S_4, (e) Li_2S_2 and (f) Li_2S.

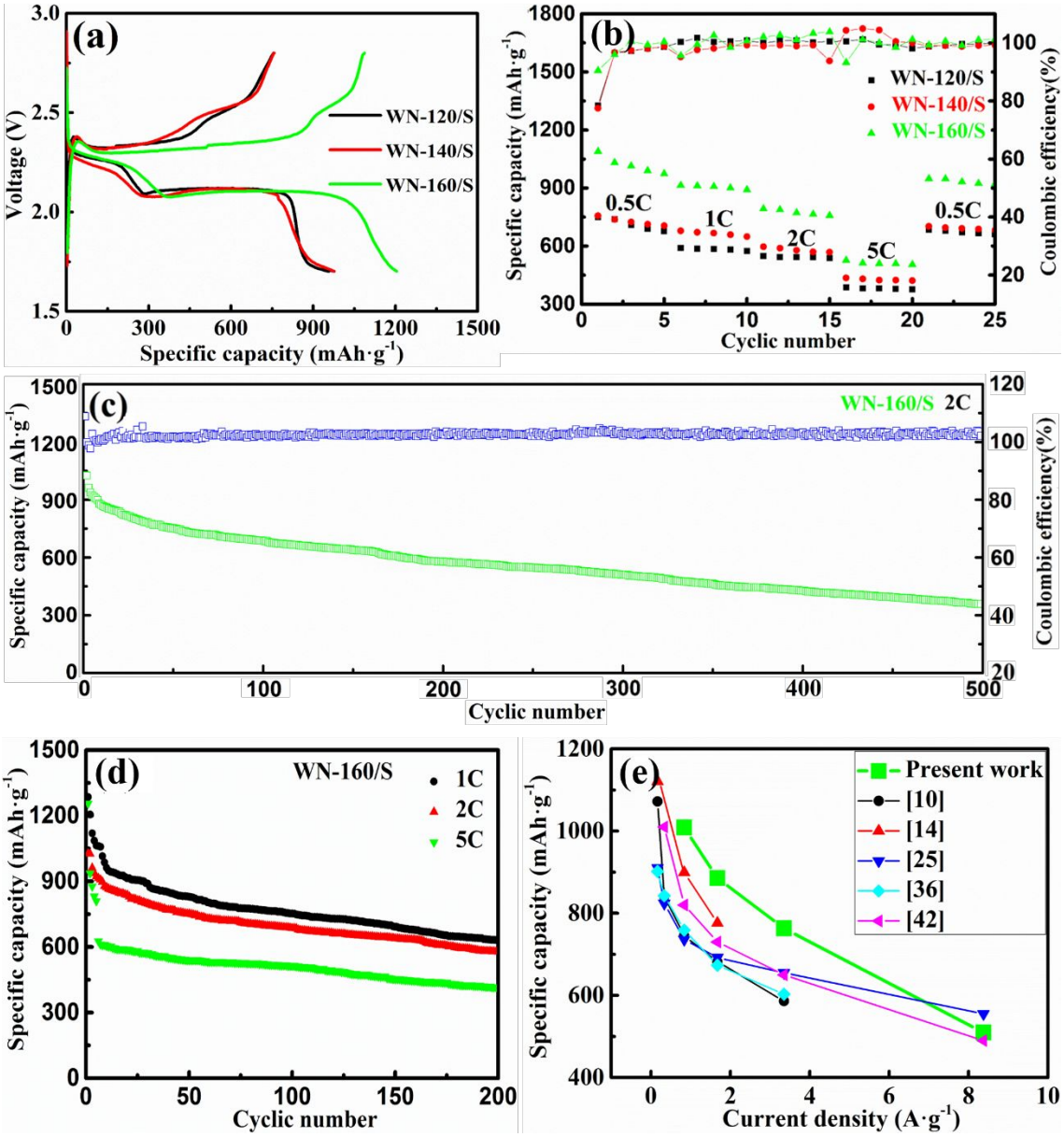

Figure 7. (a) and (b) Comparative plots of the rate capabilities and the charge/discharge profiles of sulfur composite cathodes confined in tungsten nitride (WN) (*viz*., WN-120/S, WN-140/S and WN-160/S), respectively; (c) the long-term cyclic performance at 2 C rate and (d) Rate performance of WN-160/S which exhibits the best performance among the composite cathodes tested and its cyclic performance shown in (c); (d) and (e) the benchmark plots of the electrochemical performance of WN-160/S composite cathode developed in this study with other

recently reported cathode counterparts with similar active loading of about 1 mg cm^{-2}, including TiN@CNT/S, [10] mesoporous TiN/S, [14] nano TiN powder/S, [25] hollow mesoporous TiN microspheres/S, [36] and Co-doped VN yolk-shell nanospheres@C/S. [42]

Graphical Abstract

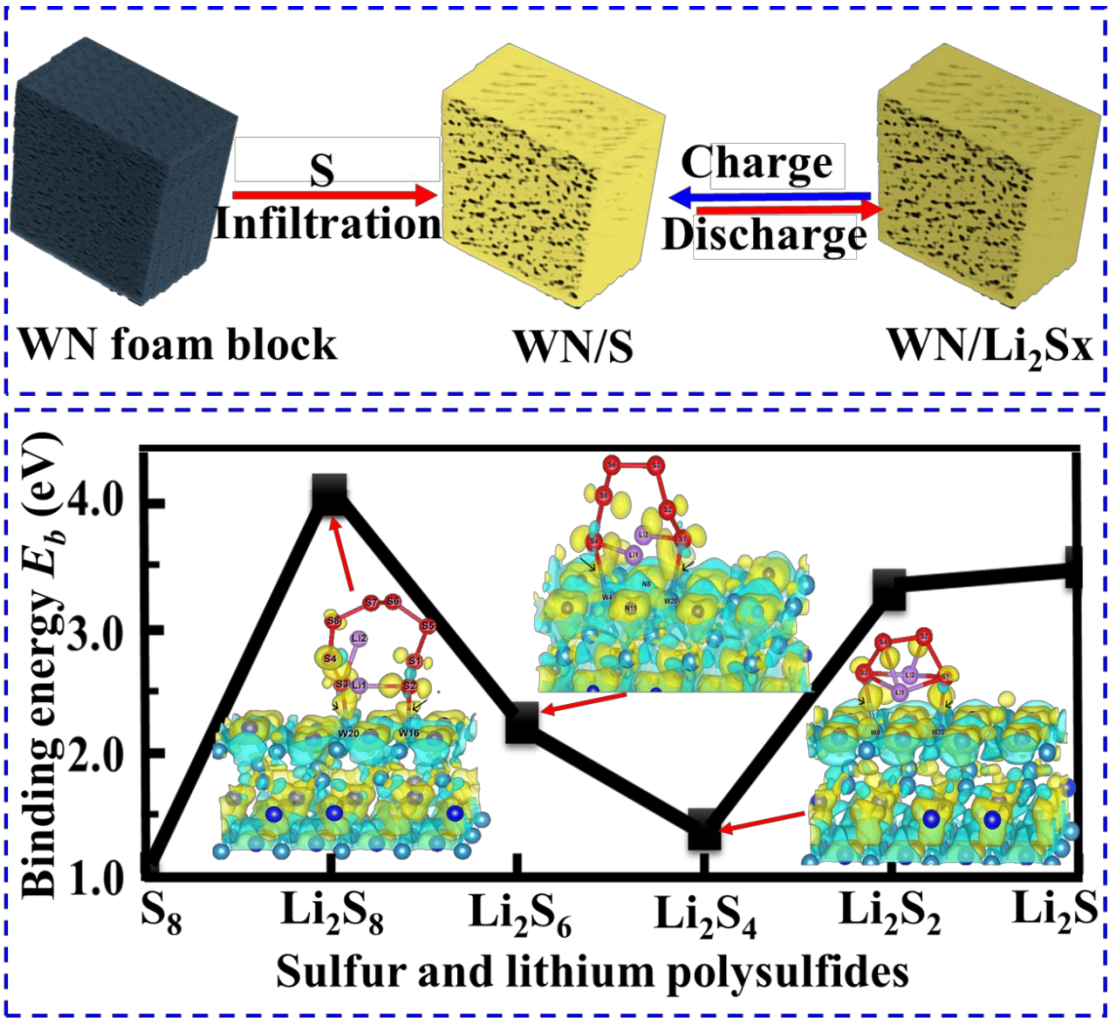

Supplementary Information

Sulfur in Mesoporous Tungsten Nitride Foam Blocks: a Rational Lithium Polysufides Confinement Experimental Design Strategy Augmented by Theoretical Predictions

Zhen-Dong Huang,[‡, a] *Yanwu Fang,*[‡, a] *Mingtong Yang,*[a] *Jike Yang,*[a] *Yizhou Wang,*[a] *Zhen Wu,**[, b] *Qingchuan Du,*[a] *Titus Masese,**[, c] *Ruiqing Liu,*[a] *Xusheng Yang,*[d, e] *Chenhui Qian,*[b] *Shaowei Jin,*[f] *Yanwen Ma**[a]

[a] Key Laboratory for Organic Electronics and Information Displays & Jiangsu Key Laboratory for Biosensors, Institute of Advanced Materials (IAM), Jiangsu National Synergetic Innovation Center for Advanced Materials (SICAM), Nanjing University of Posts and Telecommunications, 9 Wenyuan Road, Nanjing 210023, P.R. China.

[b] Shaanxi Key Laboratory of Energy Chemical Process Intensification, School of Chemical Engineering and Technology, Xi'an Jiaotong University, Xi'an 710049, P.R. China.

[c] Research Institute of Electrochemical Energy, National Institute of Advanced Industrial Science and Technology (AIST), Ikeda, Osaka 563-8577, Japan.

[d] Department of Industrial and Systems Engineering, Hong Kong Polytechnic University, Hung Hom, Kowloon, Hong Kong, P.R. China.

[e] Hong Kong Polytechnic University Shenzhen Research Institute, Shenzhen, 518057, P.R. China.

[f] National Supercomputing Center in Shenzhen, Shenzhen 518055, P.R. China.

AUTHOR INFORMATION

[‡] *Dr. Zhen-Dong Huang and Mr. Yanwu Fang contributed equally to this work.*

Corresponding Author

* E-mail address:

wuz2015@mail.xjtu.edu.cn (Z. Wu);

titus.masese@aist.go.jp (T. Masese);

iamywma@njupt.edu.cn. (Y. W. Ma)

1. Supplementary experimental information

1.1. Computational details

Theoretical calculations based on the density functional theory (DFT) approach were performed to gauge the interactions between tungsten nitride (WN) and various Li_xS_n polysulfide species (S_8, Li_2S_8, Li_2S_6, Li_2S_4, Li_2S_2 and Li_2S; lithium polysulfide products at various lithiation states of sulfur (S) cathode), using the Vienna Ab initio Simulation Package (VASP). [1, 2] During the calculations of total energy (hereafter as TOTEN), the generalized-gradient approximation (GGA)-PBE functional was adopted to estimate the exchange-correlation energy which is a critical component of the TOTEN. [3] Self-consistent field (SCF) iteration method was additionally used to solve the Kohn-Sham (K-S) equation [4] for the TOTEN calculations. During the iteration process, the Pulay mixture density [5] was chosen to effect electron relaxation in the SCF approximation protocol.

A plane wave basis set was used with a cut-off energy of 680 eV, and the Monkhorst-Pack *k*-point was set at 3×5×1 for the crystal structures involving the WN species. As for Li_xS_n polysulfide species, 400 ev and a 2×2×2 Monkhorst-Pack *k*-point mesh were chosen, respectively, as the cut-off energy and the Brillouin zone integration range. The tolerances of energy and force were set as 10^{-5} eV and 0.02 eV·Å^{-1}, respectively.

The lattice parameters of WN unit cell were set as $a = b = c = 4.130$ Å with the cubic *Pn*-3*m* space group. [6] We focused on the adsorption of various Li_xS_n polysulfides on the (200) plane surface of WN, as it has been reported to present the best adsorption

performance. [7] The corresponding (200) surface was extracted from the crystal model of WN unit cell to establish periodic slabs with three atomic layers. Among the three layers, the outermost two layers were set as full relaxation and the remaining innermost layer was fixed firmly in its position. To minimize or even ignore the interactions between the periodic slabs, a vacuum layer with a thickness of 15 Å was inserted between the slabs for the separation.

The adsorption performance of the surface can be evaluated based on the binding energy E_b which is defined as the following equation.

$$E_b = E_{WN-sur} + E_{Li_xS_n} - E_{WN-Li_xS_n} \quad (1)$$

where E_{WN-sur}, $E_{Li_xS_n}$ and $E_{WN-Li_xS_n}$ denote the TOTEN of the WN (200) surface, the Li_xS_n species and the adsorption system (WN + Li_xS_n), respectively. A positive value of E_b, corresponding to a stable adsorption system, suggests that the Li_xS_n polysulfides can be favorably adsorbed on the WN surface. Besides, a higher E_b value indicates a stronger binding interaction between the WN surface and the Li_xS_n polysulfide species.

1.2. Materials characterization

The morphology and elemental mapping of both the as-prepared precursors and final products were characterized by using field emission scanning electron microscopy (FE-SEM, Hitachi S-4800) at an acceleration voltage of 3 kV and high-resolution transmission electron microscopy (TEM, FEI Talos) at an acceleration voltage of 100 kV. Nitrogen adsorption / desorption isotherms were obtained at 77 K using an automated adsorption apparatus (Micromeritics ASAP 2020). The surface area of the

samples was calculated based on the conventional Brunauer–Emmett–Teller (BET) equation by using surface area and porosimetry analyzer (BET, V-Sorb 2800P). X-ray diffraction (XRD) patterns of the as-prepared tungstate oxides (WO-120, WO-140 and WO-160) and nitrides (WN-120, WN-140 and WN-160) were measured on an X-ray diffractometer (Bruker D8 Advance A25) using Cu–*K*α radiation (λ = 1.54060 Å). The diffraction patterns were recorded in a 2θ range of 10–80 ^{o} with a step size of 0.02 ^{o}. The polysulfide chemisorption capability of WN-Li_2S_6 and acetylene black-Li_2S_6 cathodes were characterized by using a UV/Vis spectrometer (Lambda 35). Firstly, sulfur powder and lithium sulfide (Li_2S) with a molar ratio of 5:1 was added into anhydrous tetrahydrofuran (THF) with continuous stirring at room temperature for 4 h. For the visual comparison of polysulfide absorption ability, 100 mg of WN powder or acetylene black were soaked into 3 mL of Li_2S_6 solution in an Ar-filled glove box. Optical photos were taken using a digital camera.

2. Supplementary illustration figures and experimental results

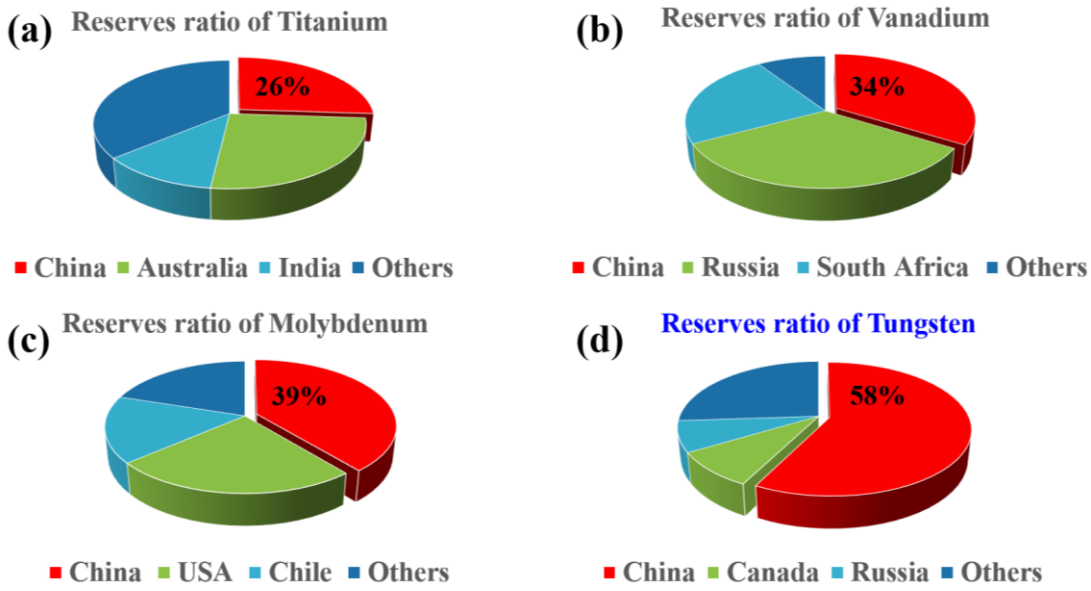

Figure S1. The main reserve holders and the corresponding reserves ratio of titanium (a), vanadium (b), molybdenum (c), and tungsten (d), respectively, summarized by referring the data from refs. 8-11.

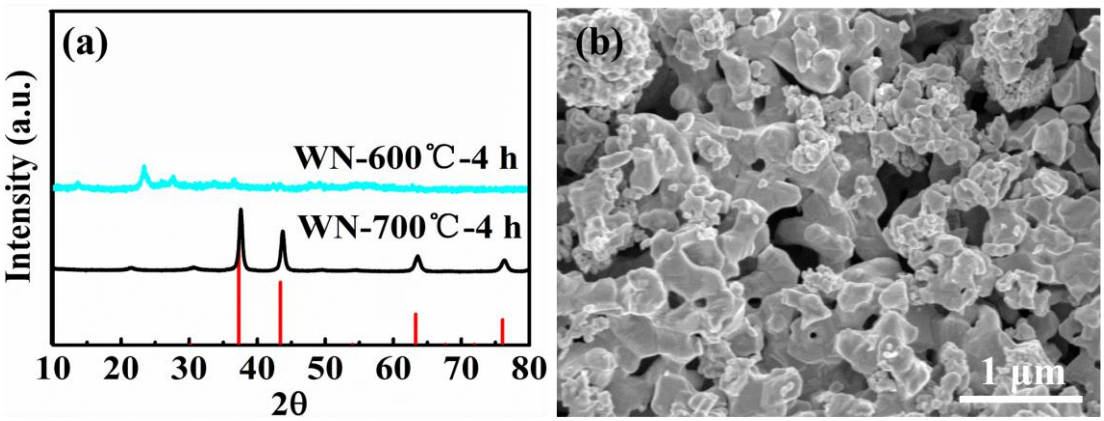

Figure S2. (a) The XRD patterns of nitride products obtained after being nitridized at 600 and 700 ^{o}C for 4 h, respectively, (b) the SEM image of nitride product obtained after being nitridized at 800 ^{o}C for 4h.

As shown in Figure S2a, the XRD pattern of nitride product obtained after being nitridized at 600 ^{o}C for 4 h could not be indexed to the standard XRD pattern of WN, but the XRD pattern of nitride product obtained after being nitridized at 700 ^{o}C for 4 h is consistant with the standard XRD pattern of WN. If the nitriding temperature was elevated to 800 ^{o}C, the obtained WN product becomes the interconnected dense particles due to the rapid growth of grains, see Figure S2b, instead of the desired mesoporous structure of tungsten nitride foam blocks. Therefore, 700 ^{o}C was finally selected as the applied nitriding temperature.

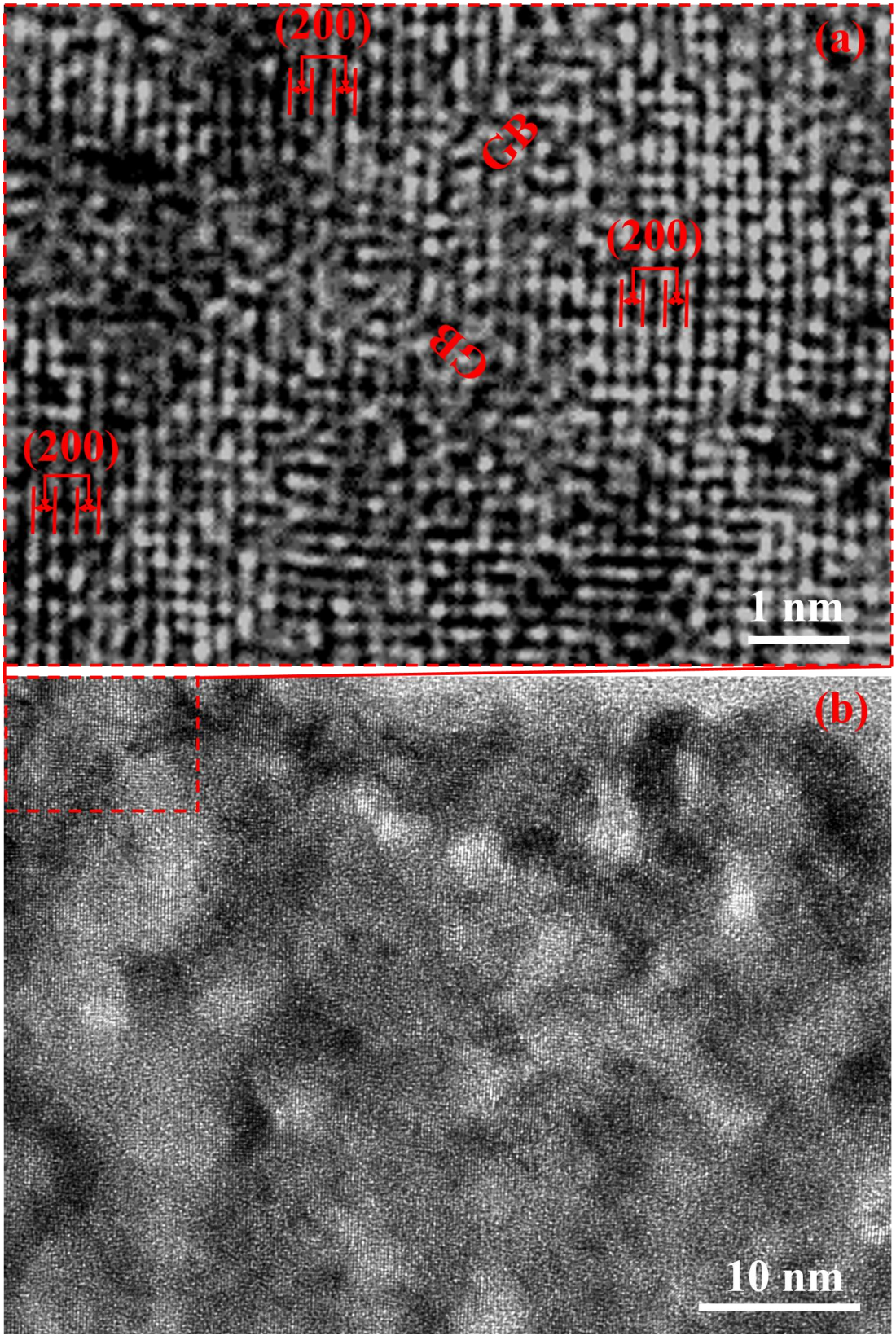

Figure S3. (a) and (b) the high resolution TEM image of the as-preapred WN-160.

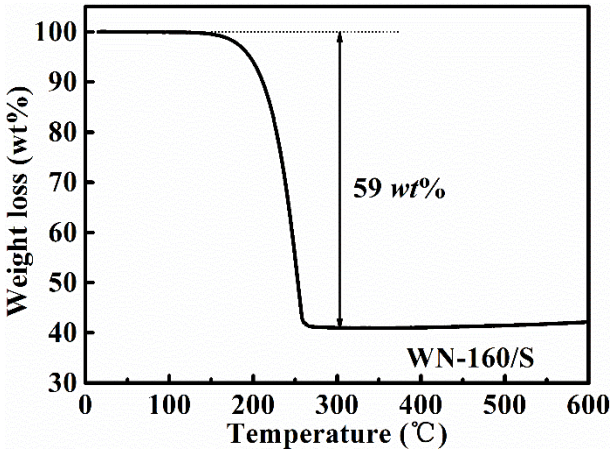

Figure S4. Thermogravimetric analysis (TG) results of the S-loaded WN-160.

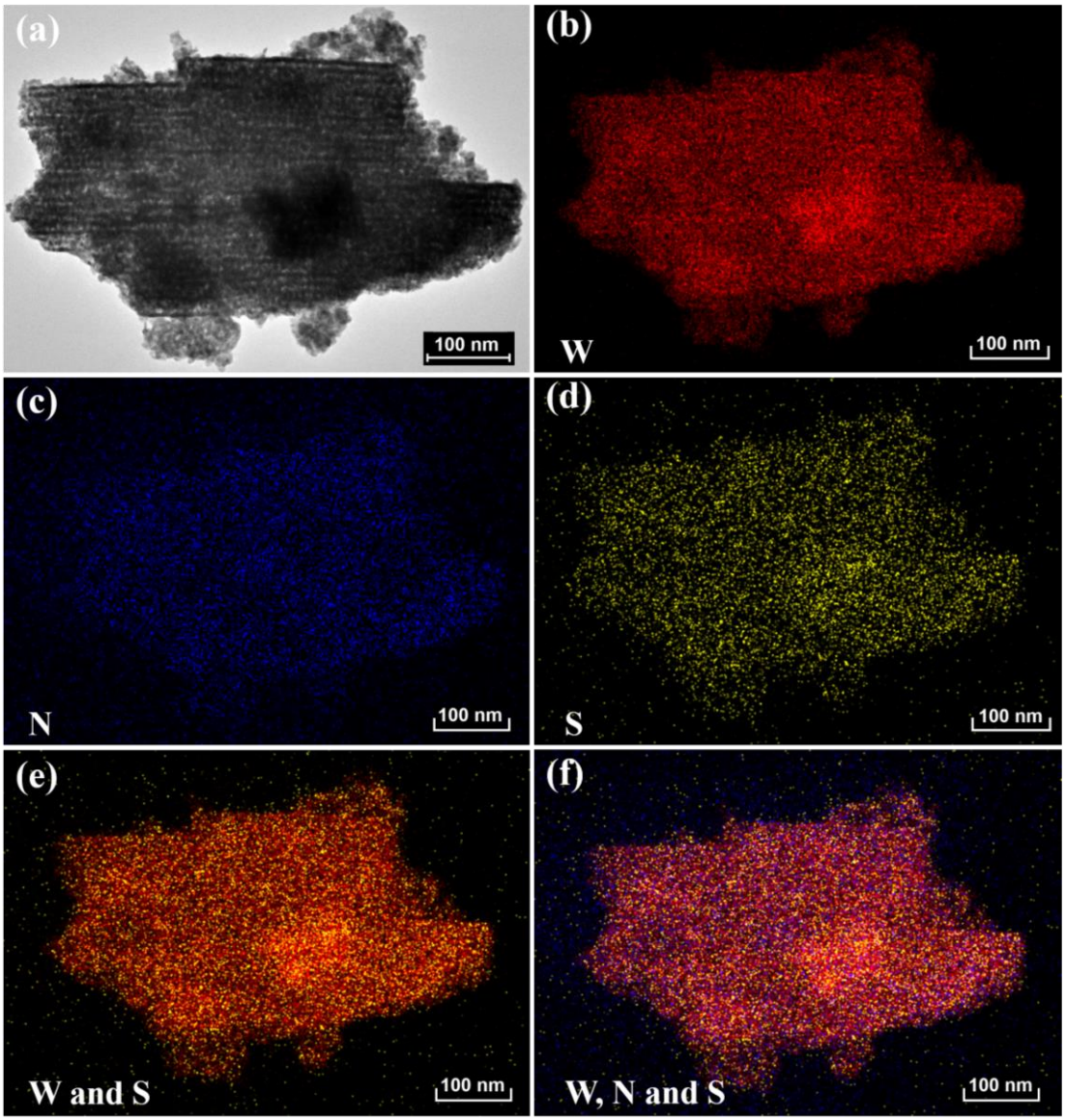

Figure S5. (a) Transmission electron microscopy (TEM) image of WN-S (sulfur confined in tungsten nitride) composites, and the corresponding elemental mapping of (b) tungsten (W), (c) nitrogen (N), (d) sulfur (S), (e) W and S combined and (f) W, N and S combined altogether.

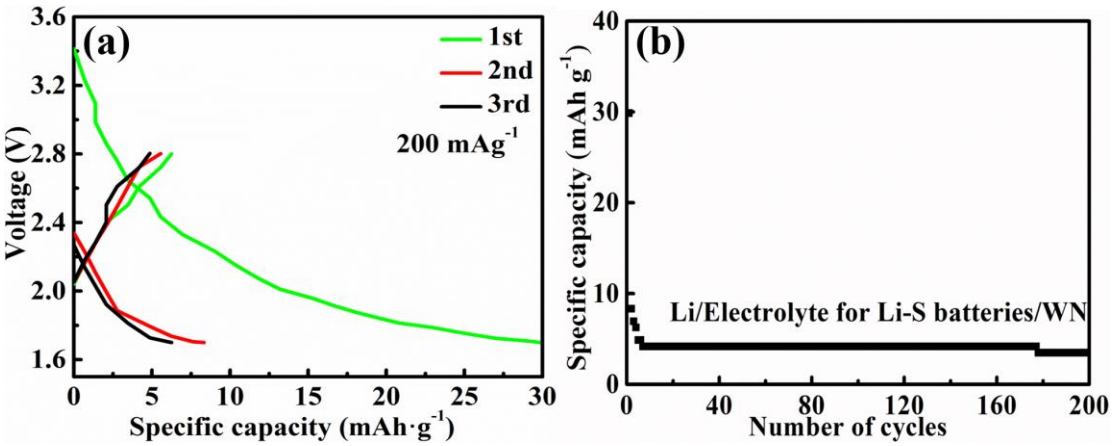

Figure S6. (a) The first three cycle charge/discharge profiles and (b) the long-term cyclic performance of the Li/electrolyte for Li-S batteries/WN-160 batteries within the electrochemical window of 1.7 ~ 2.8 V.

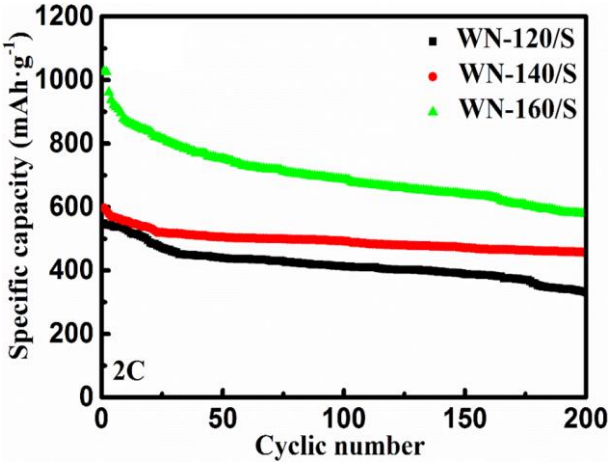

Figure S7. the cyclic performance at a 2 C rate of the lithium-sulfur batteries built with the composite cathodes of WN-120/S, WN-140/S and WN-160/S.

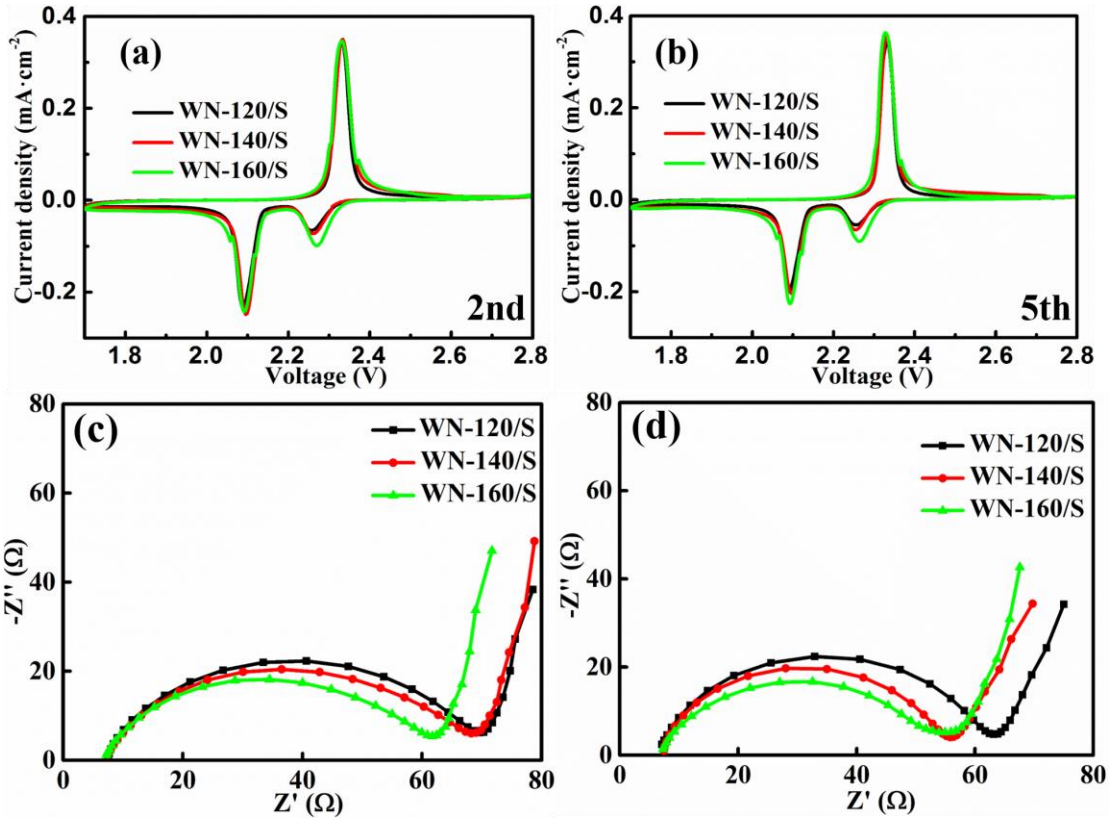

Figure S8. Cyclic voltammograms at (a) the second and (b) fifth cycles of the composite cathodes of WN-120/S, WN-140/S and WN-160/S at a scanning rate of 0.1 mV s^{-1}, (c) The EIS of WN at the initial state and (d) after fifth CV cycles of the electrode of WN-120/S, WN-140/S and WN-160/S at a scanning rate of 0.1 mV s^{-1}.

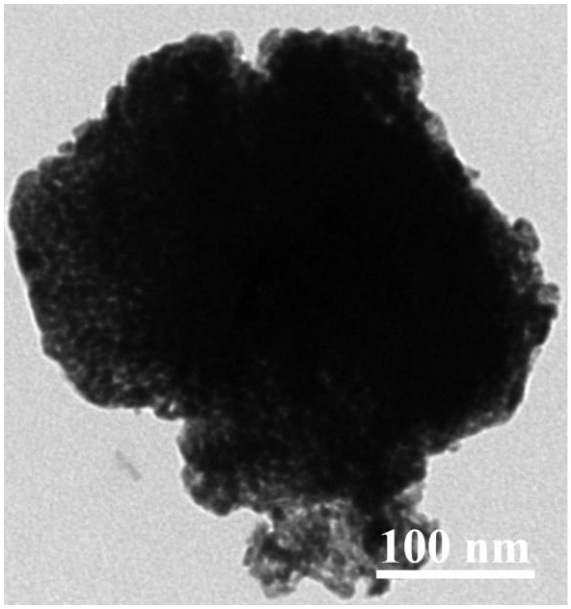

Figure S9. The TEM image of WN-160 nanoblock after 200 cycles.

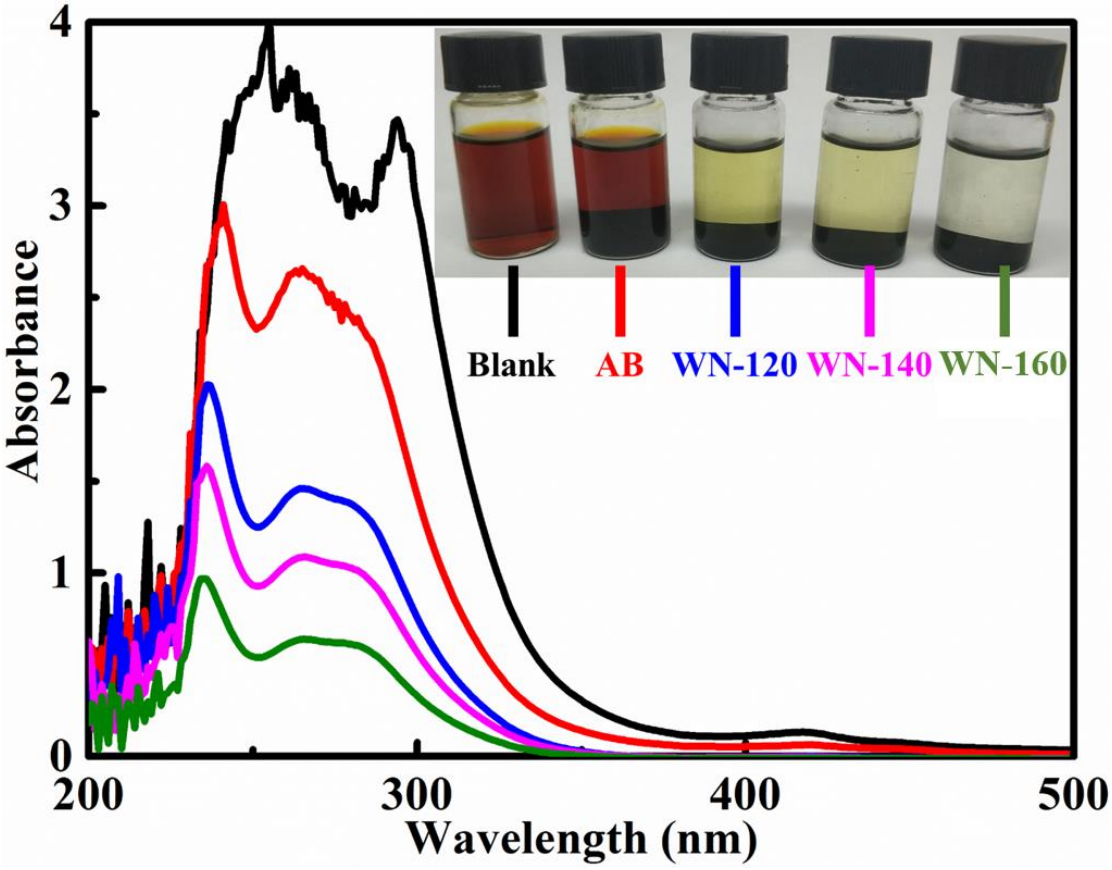

Figure S10. UV/Vis adsoption spectra of Li_2S_6 tetrahydrofuran solutions after addition of acetylene black, WN-120, WN-140 and WN-160 for 4 h. Inset shows the optical images.

References

(1) Kresse, G.; Hafner, J. Ab initio Molecular Dynamics for Liquid Metals. *Phys. Rev. B* **1993,** *47*, 558-561.

(2) Kresse, G.; Furthmüller, J. Efficiency of Ab-initio Total Energy Calculations for Metals and Semiconductors Using a Plane-Wave Basis Set. *Comput. Mater. Sci.* **1996,** *6*, 15—50.

(3) Perdew, J. P.; Burke, K.; Ernzerhof, M. Generalized Gradient Approximation Made Simple. *Phys. Rev. Lett.* **1996,** *77*, 3865—3868.

(4) Kohn, W.; Sham, L. J. Self-Consistent Equations Including Exchange and Correlation Effects. *Phys. Rev.* **1965,** *140*, A1133—A1138.

(5) Franscis, G. P.; Payne, M. C. Finite Basis Set Corrections to Total Energy Pseudopotential Calculations. *J. Phys- Condens. Mat.* **1990,** *2*, 4395—4400.

(6) Tominaga, H.; Nagai, M. Cathode Catalysts for Fuel Cell Development: A Theoretical Study Based on Band Structure Calculations for Tungsten Nitride and Cobalt Tungsten Nitrides. *Electrochim. Acta* **2009,** *54*, 6732—6739.

(7) Wang, Y. L.; Nie, T.; Li, Y. H.; Wang, X. L.; Zheng, L. R.; Chen, A. P.; Gong, X. Q.; Yang, H. G. Black Tungsten Nitride as a Metallic Photocatalyst for Overall Water Splitting Operable at up to 765 nm. *Angew. Chem. Int. Ed.* **2017,** *56*, 7430—7434.

(8) Titanium resource reserves, distribution and mineral production, Metal Encyclopedia, http://baike.asianmetal.cn/metal/ti/resources&production.shtml.

(9) Vanadium resource reserves and mineral production, Metal Encyclopedia, http://baike.asianmetal.cn/metal/V/resources&production.shtml.

(10) Molybdenum resource reserves distribution and production, Metal Encyclopedia,

http://baike.asianmetal.cn/metal/mo/resources&production.shtml.

(11) Tungsten resource distribution and production, Metal Encyclopedia, http://baike.asianmetal.cn/metal/w/resources&production.shtml.